Delft University of Technology

Faculty of Civil Engineering and Geosciences

# AESM 2006 Petroleum Engineering Master Thesis: Geothermal Energy Production From Faulted Systems with Stress-Induced Aperture Changes

*Authors:*
**Chenyang Wang (4843339)**

*Supervisors:*
**Denis Voskov**
**Alexandros Daniilidis**
**Yang Wang**

**To be defended on October 30, 2020**

# Abstract

Transition to cleaner energy while sustaining the heat demand necessity has always been an emphasized topic in the recent years. With the slowly declining utilization and production of natural gas in Netherlands, geothermal energy shows a promising future in providing sustainable power for heating and various applications. For majority of economically feasible geothermal project, either natural fractures or hydraulic fractures are present. These fractures served as a preferential fluid pathway between geothermal well couplets, which determines crucial parameters such as breakthrough time and project life.

In this study, the main focus is the impact of stochastic distribution of fracture aperture with or without pressure dependence and gravity effect on geothermal energy production. The simulation conditions as well as reservoir physical model are collected from analogous enhanced geothermal systems (EGS) that are classified as deep geothermal energy projects.

The test cases include base case, case with no pressure or stress dependence, case with half well doublet distance, and case with gravity that has well positioned in the dip or strike direction in relative to the fault orientation.

The ensemble simulation of 100 realization is run for each scenario considered. The relevant parameters analyzed are pressure difference between well couplet, production temperature, NPV, and most importantly, net cumulative energy production. It is found out that the geothermal energy production greatly relies on the fracture aperture distribution with or without pressure dependence. For base case, the range of energy production is from 1.50E13 to 3.75E13 KJ with temperature variation of 35 K between the minimum and maximum value. Without pressure dependence, only pressure difference between injector and producer slightly changes, and production temperature as well net energy production remains nearly identical. For the case with half of original well-spacing, the spread of energy production distribution reduces from 1.50E13 to 3.25E13 KJ. The diminishing energy production results from less total enthalpy in the flow path with shorter distance, yet the outcome of energy production still demonstrates a considerable range.

By taking account of gravity effect and populate the reservoir with non-uniform pressure and temperature distribution with corresponding gradient, the net energy production drops to approximately two times less than the base case. However, the ratio of maximum energy production to the minimum over 100 realization is similar to that of the base case. Last but not least, two types of well orientation, along the strike and along the dip of fracture plane, are considered to observe the impact of gravity-assisted flow. It is concluded that with the current model setting, the low temperature gradient of injector in the dip configuration case overweighs the effect of gravity assistance, resulting in a smaller net energy production than the strike case.

This project concludes that the fracture aperture heterogeneity is an important factor in predicting the outcome of deep geothermal production. The gravity is another crucial component to portray accurate flow behavior between the wells, but it does not result in additional increase in the range of energy production outcome in comparison to the base come with the simulation conditions applied.

i

# Contents

$1$

# Introduction

## 1.1. Background Info

Current potential of geothermal energy is immeasurable with active R&D program from oil and gas industry as well as subsidy from the regulation agencies. Based on the recent climate agreement, the Netherlands is aiming to reduce the equivalent $CO_2$ emission by approximately 40 % before 2030 and 95 % by 2050 relative to the emission level in 2015, which correspondingly translates to 20 ans 36 mega-tones of $CO_2$ emission (SPG, 2018). To achieve this goal, geothermal energy is considered as one of the diversified sustainable energy mix in the future. It is believed that with the existing and planned geothermal projects, geothermal energy can contribute up to 23 % of the total heat demand in 2050 (SPG, 2018).

Although the future development of geothermal energy seems to be optimistic, uncertainties arise in geothermal reservoir simulation to generate accurate predictions. The main focus of this study is the impact of fracture plane aperture distributions on energy output and other relevant parameters.

Due to the complex nature of subsurface sedimentary processes, the fracture/fault plane has usually complex heterogeneous structure. In previous studies related to characterization of fracture flow patterns (Wu, H. et al, 2019), it is observed that although the channelized feature of flow is more common in nature fracture than hydraulic fracture, the correlation between aperture distribution and flow patterns in the fracture is nearly non-existent. Another study focuses on a slow immiscible displacement capillary pressure behavior associated with degree of fracture aperture heterogeneity (da Silva et al, 2019). It states that the natural fractures distinguishes from porous media significantly due to its varying roughness degrees as well as self-affine correlation structure. Since it is impossible to know the fracture aperture exactly, the aperture in our study will be generated as a stochastic field following the study of fracture drainage invasion precolation models (Yang et al, 2012) and horizontal rough-walled fracture drainage investigation (Neuweiler et al, 2004). The detailed parameters for fracture aperture distribution and the model setup will be explained in the subsequent chapters.

## 1.2. Definition of Geothermal Systems

In a general sense, geothermal energy becomes available from the depth of several hundred meters down to 4000 meters or even more. The essential component of a recoverable geothermal system including heat source, porous rock, fluid pathway and seal. There are three sub-categories in the geothermal family, namely shallow geothermal energy (300 to 1500 m), deep geothermal energy (1500 to 4000 m) and ultra-deep geothermal energy (4000 to 8000 m) (ThermalGIS, u.d.). At shallow depths, storage system such as aquifer thermal energy storage (ATES) prevails due to the high heat capacity of the rocks. With a deeper depth, the produced hot water can be used for direct heating of buildings and green houses.

Enhanced geothermal system contains hydraulic fractures often stimulated for a better connectivity between wells. This type of systems is frequently observed in the deep or ultra deep formations as the porous space within the rock is reduced with higher overburden stress at greater depth. In other word, geothermal reservoir that possess sufficient temperature potential yet lack of sufficient permeability is a suitable candidate for the development by EGS application (DiPippo, 2016).

Another useful way of viewing different geothermal systems is to put them on a spectrum based on the relationship between formation permeability and temperature. As shown in Figure 1.1 (Thorsteinsson et al, 2008), a high formation permeability with an average geothermal gradient of 30 °C leads to a low-grade hydro-thermal system. On the left side of the plot, one can find systems with moderate to insufficient permeability, and in these cases, EGS systems are available for possible economic heat extraction.
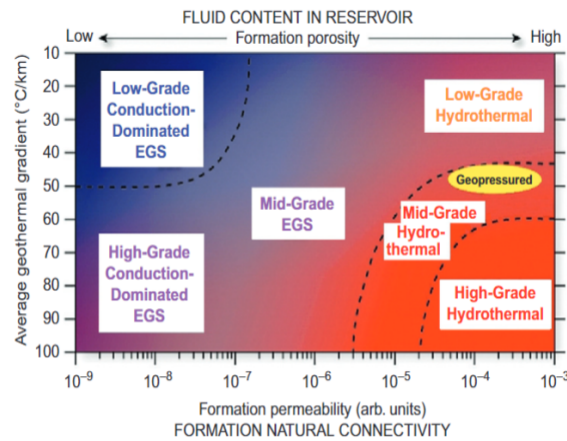


Figure 1.1: Geothermal System Spectrum

## 1.3. Research Tools

The grid structure of reservoir and specific aspects of fractures such as its orientation, layering, thickness, length and resolution are constructed with Gmsh. The generated Gmsh file is then exported to the Delft Advanced Research Terra Simulator (DARTS) (Khait, 2019) with the update geothermal module to run simulations under determined conditions. The DARTS is run in Python and simulation results at each determined time step are then exported to VTK files and can be visualized in ParaView.

A visualized example of fracture grid within its matrix in Gmsh is shown in Figure 1.2 below. Note that the block size in x and y direction depends on the preset fracture resolutions.



Figure 1.2: Fracture within the matrix system

Figure 1.3: Fracture on 2D Plane View

## 1.4. Existing Deep Geothermal Projects Geology and Reservoir Condition

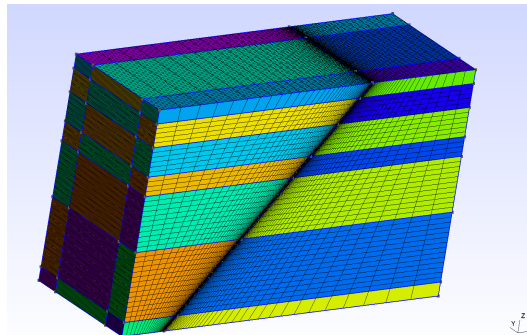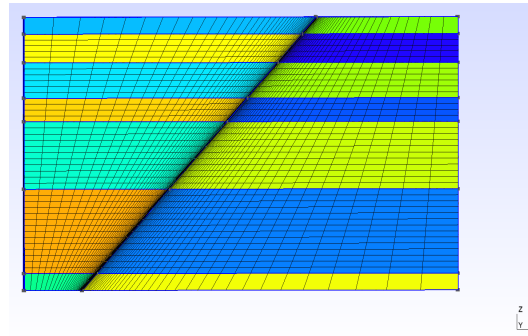The two deep geothermal projects that will be used as an analogy for simulation conditions in this project are Soultz-sous-Forets and Rittershoffen project located at Upper Rhine Graben.

### 1.4.1. Soltz-sous-Forets Geothermal Project

Started in 1987, the Soultz-sous-Forets geothermal project is the pioneer for laying the groundwork to research European geothermal system in fracture granitic reservoir. It is located in Northern Alsace, France on top of the Upper Rhine Graben about 6km North-West of Rittershoffen project as indicated in Figure 1.4(Baujard et al, 2017). The project operation commenced in 2016 and has since been in continuous exploitation successfully with its installed gross capacity of 1.7 $MW_e$ (Geoenvi, 2020).
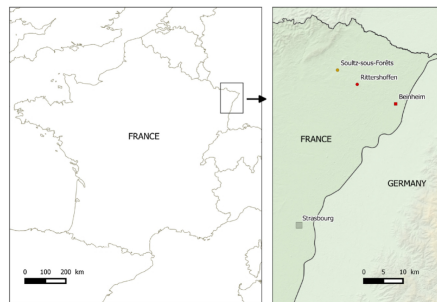


Figure 1.4: Location of Soltz-sous-Forets Geothermal Project

The Soultz-sous-Forets geothermal reservoir is characterized by the low-permeability granitic zones that requires hydraulic stimulation for feasible energy production. The Paleozoic granite is found in crystalline basement located 1.4 km below the sedimentary layers, and it is highly fractured at both micro-scale and fracture or fault zones (Vidal & Genter, 2018). Two distinct granitic units are present in the subsurface up to a depth of 5 km. The porphyritic monzo-granite is found at depth of 4.5 km with the fine-grained biotite-muscovite granite right below (Vidal & Genter, 2018).The natural fracture within the fractured zone can have a thickness from 10 to 20 m (Genter et al, 2010). Approximately 40 fault zones has been found in the granite and the dominant strike direction is N160°E (Genter et al, 2010). A cross section includes both Soultz-sous-Forets and Rittershoffen project along with the major fault presence is shown in Figure 1.5 below (Vidal & Genter, 2018). A detailed introduction for Rittershoffen project will be given in the next section.

(a) NW-SE Cross Section Perpendicular to the Graben          (b) Cross Section Legend

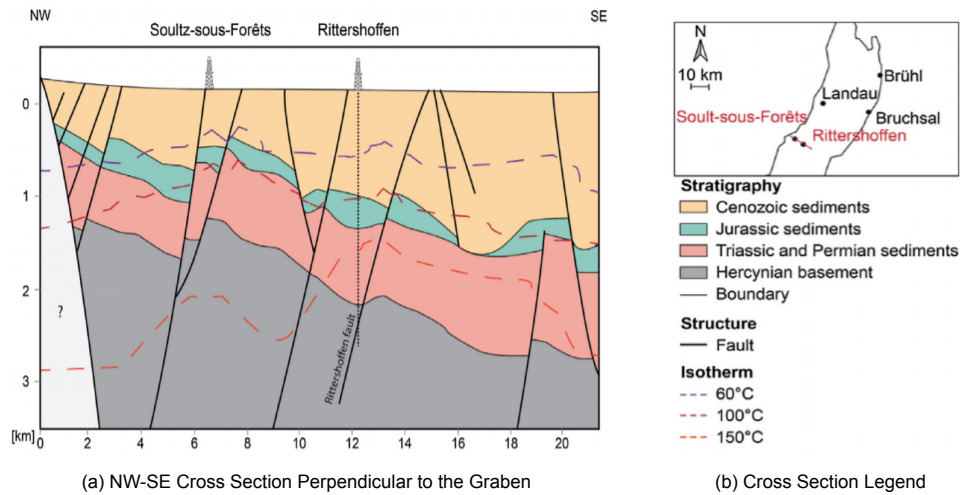Figure 1.5: Pressure Variation Along 2D Reservoir

The geothermal system is consists of 1 production well and 2 injection wells, and the injected brine reaches the production wellhead at 150 °C and 23 bar with the subsequent re-injection temperature set at 70 °C (Moucho et al, 2018). Some relevant reservoir properties collected from the recent BINE report (BINE, n.d.) is summarized in the table 1.1 below.

| Parameters | Value |
|---|---|
| Reservoir Depth | 5000 (m) |
| Reservoir Dimension (x, y, z) | 3500 * 4500 * 500 (m) |
| Reservoir Temperature | 200 (Deg) |
| Reservoir Pressure | 500 (Bar) |
| Injection Water Temperature | 70 (Deg) |

Table 1.1: UDG Reservoir Simulation Condition: Soultz-sou-Forets

## 1.4.2. Rittershoffen Geothermal Project

Similar to the Soltz-sous-Forets project, the Rittershoffen project is also located at the Upper Rhine Graben (URG) in Northeast France. The potential of geothermal energy production is great in URG due to local thermal anomalies along with the presence of a dense fractured network. Along with the Soultz-sous-Forez project, the Rittershoffen geothermal project started its production for industrial super-heated water in 2016 with a total estimated capacity of 24 $MW_{th}$ (Baujard, 2018). The field has gone through 3 phases of development, which are correspondingly thermal, chemical and hydraulic stimulation. The chemical stimulation aims to dissolve sealing minerals in the fractures and the hydraulic stimulation quantified the effect of chemical stimulation (Baujard, 2018).

The Rittershoffen field lies on Rittershoffen fault, which is a normal fault with orientation of N45°E located 15 km east of the Western Rhenane border fault (Baujard, 2017). For the simulation model, it is assumed to be a five-layer structure with the fault strike angle of North-South and dip angle of 45°W. The fault ends at the depth of 3250 m. A scheme of the describe model is displayed below in Figure 1.6 with the rock properties of each layer presented in Table 1.2 (Daniilidis, u.d.).
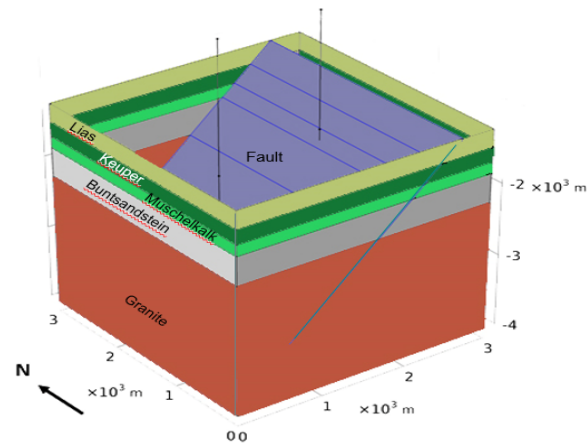
Figure 1.6: Rittershoffen Project Reservoir Model with the Rittershoffen Fault (Note that the location of injection and production well can be altered as part of sensitivity analysis)

|  | Lias | Keuper | Muschelkalk | Buntsandstein | Granite | Fault |
|---|---|---|---|---|---|---|
| **Porosity, -** | 0.04 | 0.044 | 0.024 | 0.096 | 0.03 | 0.25 |
| **Permeability, mD** | 0.37 | 0.55 | 0.7 | 2.33 | 5.15 | 53.4 |
| **Density, kg/m^3** | 2390 | 2390 | 2390 | 2390 | 2630 | 2630 |
| **Heat Capacity, J/ (kg*K)** | 1006 | 1016 | 1021 | 573 | 828 | 828 |
| **Thermal Conductivity, W/(m*K)** | 2.5 | 1.9 | 2.3 | 2.3 | 3.0 | 3.0 |

Table 1.2: Rittershoffen Reservoir Rock Properties for Simulation

A complete chrono-stratigraphic log of the Rittershoffen reservoir is displayed below, with data of thickness and main geological feature referring to Figure 1.6 (Duringer, 2019).



Figure 1.7: Rittershoffen Reservoir Gamma-Ray Log with Detailed Lithology

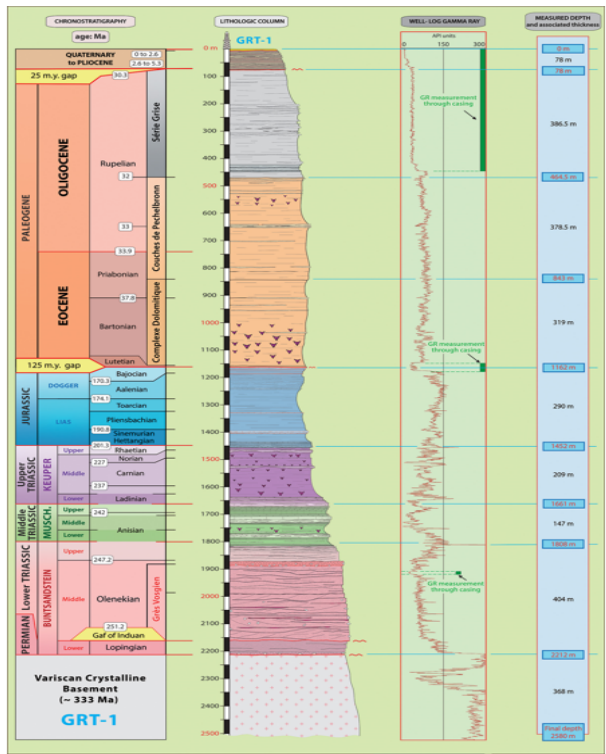| Formation | Thickness (m) | Geological Features |
|---|---|---|
| Lias | 170 | clay-dominant with minor presence of limestone bank and marls |
| Keuper | 210 | mainly clayey, marly and dolomitic with some thin beds of sandstone |
| Muschelkalk | 140 | marl and limestone alteration, dolomites and dolomitic marls |
| Buntsandstein | 400 | fine to coarse-grained continental sandstone with some conglomeratic beds |
| Variscan Basement | >1000 | mainly granite with presence of biotite, chlorite, feldspar and quartz |

Table 1.3: Model Parameters and Geological Features

For the simulations, the physical model is established based of the Rittershoffen layer scheme as shown in Figure 1.6 and the simulation conditions will be taken both from Soultz-sous-Forets and Rittershoffen projects, with appropriate change of reservoir temperature and pressure based on the model depths. For each layer of lithology in the reservoir matrix, corresponding rock properties are assigned individually according to Table 1.2. A detailed discussion for the simulation condition and set-ups is provided at the beginning of "Results" Chapter.

# 2

# Theory and Methodology

## 2.1. Governing Equations

The governing equations reflects the physical conservation laws in the simulation to describe transfer of mass and energy. In a multi-component system, the mass conservation equation for system with $n_p$ phases and $n_c$ component can be expressed as:

$$\frac{\delta}{\delta t}(\phi \sum_{p=1}^{n_p} x_{cp}\rho_p s_p) + div \sum_{p=1}^{n_p} x_{cp}\rho_p \vec{u}_p + \sum_{p=1}^{n_p} x_{cp}\rho_p \tilde{q}_p = 0, \quad \text{for c} = 1, ..., n_c. \tag{2.1}$$

In Equation 2.1 (Khait, 2019) above, $\phi$ represents effective porosity, $\rho_p$ is phase molar density, $x_{cp}$ is the concentration of component c in phase p, $s_p$ is phase saturation, $\vec{u}_p$ is phase velocity and $\tilde{q}_p$ is the phase source term.

The phase velocity mentioned above is calculated from Darcy's Law, in which:

$$\vec{u}_p = -(K \frac{k_{rp}}{\mu_p}(\Delta p_p - \gamma_p \Delta D)). \tag{2.2}$$

In Equation 2.2 (Khait, 2019) K represents effective permeability, $k_{rp}$ is phase relative permeability, $\mu_p$ is phase viscosity, $\gamma_p$ is phase pressure gradient in vertical direction and D stands for depth.
Similarly, the energy conservation equation takes the form of:

$$\frac{\delta}{\delta t}(\phi \sum_{p=1}^{n_p} \rho_p s_p U_p + (1 - \phi)U_r) + div \sum_{p=1}^{n_p} h_p \rho_p \vec{u}_p + div(\kappa \Delta T) + \sum_{p=1}^{n_p} h_p \rho_p \tilde{q}_p = 0. \tag{2.3}$$

A few new terms are seen in Equation 2.3 (Khait, 2019) compare to Equation 2.1, which are mostly the heat terms. Specifically, $U_p$ is the phase internal energy, $U_r$ represents rock internal energy, $h_p$ is thermal enthalpy and $\kappa$ is thermal conduction.

To solve both of the conservation equations, the fully implicit finite-volume discretization is applied to Equation 2.1 and Equation 2.3. The corresponding discretized form is:

$$V((\phi \sum_{p=1}^{n_p} x_{cp}\rho_p s_p) - (\phi \sum_{p=1}^{n_p} x_{cp}\rho_p s_p)^n) - \Delta t \sum_l (\sum_{p=1}^{n_p} x_{cp}^l \rho_p^l \Gamma_p^l \Delta \psi^l) + \Delta t \sum_{p=1}^{n_p} x_{cp}\rho_p q_p \quad \text{for c} = 1, ..., n_c, \tag{2.4}$$

$$V((\phi \sum_{p=1}^{n_p} \rho_p s_p U_p) - (\phi \sum_{p=1}^{n_p} \rho_p s_p U_p)^n) - \Delta t \sum_l (\sum_{p=1}^{n_p} h_p^l \rho_p^l \Gamma_p^l \Delta \psi^l) + \Delta t \sum_{p=1}^{n_p} h_p \rho_p q_p. \tag{2.5}$$

In Equation 2.4 and Equation 2.5 (Khait, 2019) above, V represents the total volume of mesh grid. $\Gamma_p^l$ is phase transimissiblity over interface l, which is simply calculated as $\Gamma^l k_{rp}^l / \mu_p^l$, and $\Gamma^l$ is the geometrical transmissibility that depends on the control volumes associated with the interface l. Additionally, $\triangle \psi^l$ is pressure difference across the interface without taking capillary and gravity effect into account.

Since for geothermal simulation a single component of water is assumed, the only unknown to solve is pressure for the mass conservation equation. For the energy conservation equation, both pressure and enthalpy need to be solved. For linearization of nonlinear system of equations, Newton-based method is applied for assembling the Jacobian and residual (Voskov, 2017). The linearization solves following system of equations for each iteration, in which $J(x^k$ is the Jacobian of iteration k and $r(x^k$ is the corresponding residual

$$J(x^k)(x^{k+1} - x^k) + r(x^k) = 0. \tag{2.6}$$

For the recently introduced Operator Based Linearization (OBL) method, the discretized conservation equations is changed into an operator form that separates spatially-dependent and state-dependent variables (Voskov, 2017). One type of operators contains physical state as well as fluid properties, while the other operators includes space-dependent parameters and the remaining state-dependent properties. The formulation of the OBL operator will be discussed in detail in the next section,

## 2.2. Variation of Permeability and Transimissiblity

The final transmissibility from DARTS simulator (Khait, 2019) of connecting fracture cells is calculated as following:

$$\Gamma_{frac} = D * \Gamma_{thermal} * \Gamma_{connection}. \tag{2.7}$$

Here, $D$ is the Darcy constant and is defined as 0.008523 with the units applied in the simulation, $T_{thermal}$ is the thermal transmissibility that can also be considered as the geometric coefficient, and $T_{connection}$ is the connection transmissibility calculated based on the permeability of neighbouring cells. Specifically, the thermal transmissibility for an interface shared by n cells can be expressed as:

$$\Gamma_{thermal} = \frac{A}{\Delta x_1 + \Delta x_2 + \ldots + \Delta x_n}. \tag{2.8}$$

In Equation 2.8, $A$ represents interface area between two connecting cells and $\triangle x$ is the distance of centroid of each cell to the mutual interface with other cells.

Furthermore, the connection transmissibility of an interface intersected with n cells is defined as:

$$\Gamma_{connection} = \frac{((A * k_1/\Delta x_1) * (A * k_2/\Delta x_2))}{A * k_1/\Delta x_1 + A * k_2/\Delta x_2 + \ldots + A * k_n/\Delta x_n}. \tag{2.9}$$

The fracture permeability is calculated based on the parallel plate model with the presence of a single fracture. In Equation 2.9, k is permeability of cells, which can be defined from the fracture aperture as (Zhang, 2019):

$$k_f = \frac{d_f^2}{12}. \tag{2.10}$$

The effective stress is obtained from the total stress and pore pressure or fluid pressure (Stress in the ground, u.d.):

$$\alpha_{eff,normal} = \alpha_m - \alpha_p. \tag{2.11}$$

Referring from Equation 2.7 to Equation 2.9, the change of permeability from stress can be implemented by adding a multiplier at the end of the transmissibility:

$$\Gamma(k^i, k^j, \alpha^{i,j}) = \Gamma(k^i, k^j) * \Gamma^m(\alpha^{i,j}). \tag{2.12}$$

At the interface, the stress value is simplified to be the average of the two interested cells:

$$\alpha^{i,j} = \frac{\alpha_i + \alpha j}{2} \tag{2.13}$$

For the aperture change induced by stress, it should slow down in high pressure range when reaching the limit, resulting in the rate of change for permeability to gradually decrease. Furthermore, an empirical study performed on artificially fractured granite rocks that focuses on the impact of confining pressure on fracture aperture demonstrates that, with 6 samples of rock at different temperature condition and test pressure range of 20 MPa, the range for fracture aperture addition is approximately 5 % to 25 % (Luo et al, 2017). Therefore, for the current reservoir simulation condition, which will create a pressure difference over 10 MPa (100 bar) over time within the reservoir, it is safe to assume a maximum aperture increase of 10 %, which translates to a maximum permeability increase of 21 %.

A suitable function to represent the pressure-perm relationship as described above can be a logarithmic expression. The multiplier has the following form:

$$K = \begin{cases} K_0 & \text{if P} <= P_{min} \\ K_0 * (1 + \log(\frac{P}{P_{min}})) & \text{otherwise} \end{cases}. \tag{2.14}$$

Where $K_0$ represents the initial permeability distribution at predetermined minimum pressure $P_{min}$. The plot for non-linear relationship is shown in the Figure 2.1.
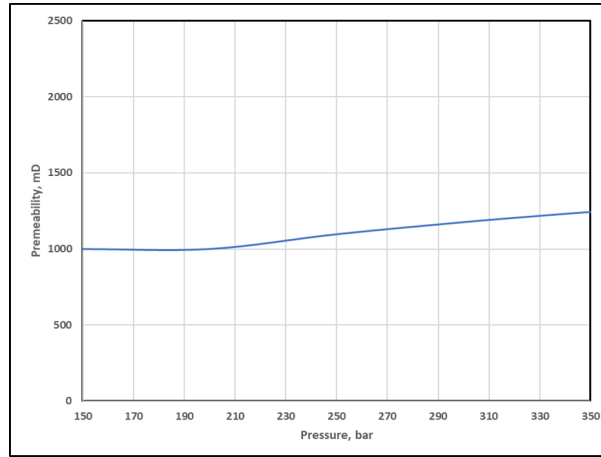


Figure 2.1: Non-Linear Permeability-Pressure Correlation Example

As it can be observed in the Figure 2.1, the permeability increases at a slower rate in the high pressure range for non-linear expression, which is expected in the real life scenario. Also, the permeability addition is approximately 20 % at the assigned maximum pressure of 330 bar, which checks out with the previous assumption for maximum permeability increase of 21 %. Therefore, for consequent simulation runs, the non-linear correlation in Equation 2.14 will be applied.

# 3

# Projection of Fault Aperture

This chapter describes some technique for projection of fault aperture from 2D sampling in Cartesian grid to the fault plane 3D unstructured grid.

## 3.1. Projection Mathematics

Although the fracture plane is considered a 2D entity in the mesh, its coordinates are still expressed in 3D in the unstructured model. Therefore, it is necessary to convert these coordinates as normalized 2D coordinates for convenience of projection since in sensitivity study, we don't want to rebuild an entire discretization for sampling of aperture distribution.
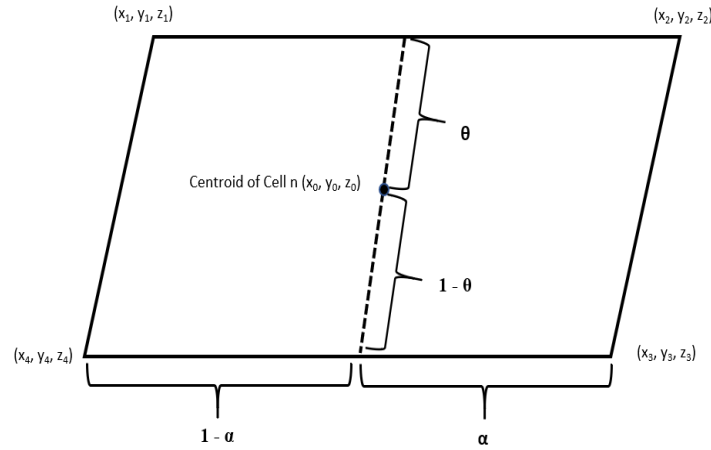
Figure 3.1: Projection for normalized x coordinates

As Figure 3.1 shows, assuming the boundary coordinates on the corners of the fracture plane and the centroid of certain fracture cell $n$ are known. In order to find the normalized $x$ coordinates $\alpha$ for the centroid, the following formulation is applied.

For the x coordinates:

$$x_{upper} = x_2\alpha + x_1(1 - \alpha)$$
$$x_{lower} = x_3\alpha + x_4(1 - \alpha)$$
$$x_0 = x_{upper}\theta + x_{lower}(1 - \theta)$$

For the y coordinates:

$$y_{upper} = y_2\alpha + y_1(1 - \alpha)$$
$$y_{lower} = y_3\alpha + y_4(1 - \alpha)$$
$$y_0 = y_{upper}\theta + y_{lower}(1 - \theta)$$

Combine these two systems of equations, we obtain:

$$x_0 = (x_2\alpha + x_1(1 - \alpha))\theta + (x_3\alpha + x_4(1 - \alpha))(1 - \theta)$$
$$y_0 = (y_2\alpha + y_1(1 - \alpha))\theta + (y_3\alpha + y_4(1 - \alpha))(1 - \theta)$$

In the non-linear system above, the only unknowns are $\alpha$ and $\theta$. It can be solved with Newton-Raphson method, which will be described in detail in the next section.

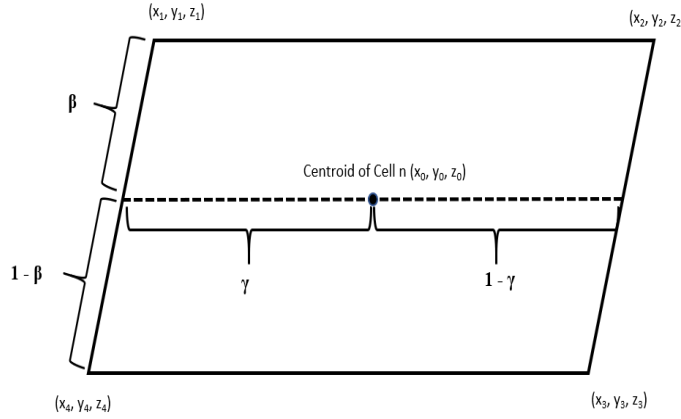The same method can be applied to obtain the normalized y coordinates $\beta$ for each cell's centroid.



Figure 3.2: Projection for normalized y coordinates

The final system of equations is:

$$x_0 = (x_1\beta + x_4(1 - \beta))\gamma + (x_2\beta + x_3(1 - \beta))(1 - \gamma)$$
$$y_0 = (y_1\beta + y_4(1 - \beta))\gamma + (y_2\beta + y_3(1 - \beta))(1 - \gamma)$$

## 3.2. Nonlinear solution

Assemble the Jacobian is an essential step in Newton-Raphson method. For example, the matrix for solving normalized x coordinate is shown as below:

$$\begin{bmatrix} \dfrac{dx_0}{\alpha} & \dfrac{dx_0}{\theta} \\ \dfrac{dy_0}{\alpha} & \dfrac{dy_0}{\theta} \end{bmatrix}.$$

Starting with an initial guess for the unknowns, the Newton-Raphson updates nonlinear unknowns following
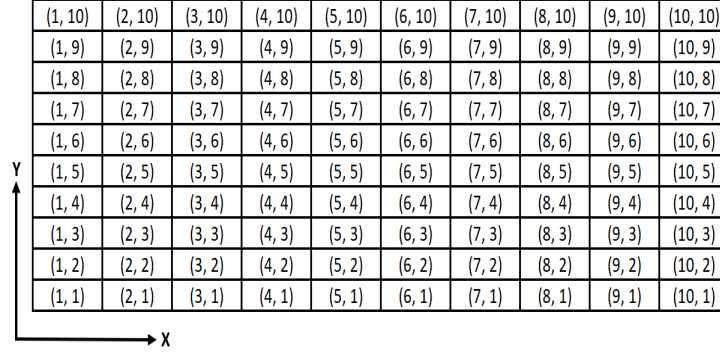
$$x^{k+1} = x^k - J^{-1}(x^k)f(x^k),$$
$$J(x^k)\delta x^k = -f(x^k),$$

where the $x^{k+1}$ is the solution at current iteration, $x^k$ is the solution at previous iteration, J is the Jacobian matrix and $\delta x^k$ is the update. The algorithm ends when $\delta x^k$ is smaller than a predetermined tolerance.

## 3.3. Projection Criterion

In order to restore the feature of the projection plane to the fracture plane in 3D coordinates as accurately as possible, it is crucial to determine the criterion to assign values on each cells within the fracture.

In the previous section, the normalized x coordinate $\alpha$ and y coordinate $\beta$ are obtained. Before the 2D projection plane is generated, it will take an input of the field resolution in form of x resolution by y resolution. As an example, a 10 by 10 field is shown in Figure 3.3.

| (1, 10) | (2, 10) | (3, 10) | (4, 10) | (5, 10) | (6, 10) | (7, 10) | (8, 10) | (9, 10) | (10, 10) |
|---------|---------|---------|---------|---------|---------|---------|---------|---------|----------|
| (1, 9)  | (2, 9)  | (3, 9)  | (4, 9)  | (5, 9)  | (6, 9)  | (7, 9)  | (8, 9)  | (9, 9)  | (10, 9)  |
| (1, 8)  | (2, 8)  | (3, 8)  | (4, 8)  | (5, 8)  | (6, 8)  | (7, 8)  | (8, 8)  | (9, 8)  | (10, 8)  |
| (1, 7)  | (2, 7)  | (3, 7)  | (4, 7)  | (5, 7)  | (6, 7)  | (7, 7)  | (8, 7)  | (9, 7)  | (10, 7)  |
| (1, 6)  | (2, 6)  | (3, 6)  | (4, 6)  | (5, 6)  | (6, 6)  | (7, 6)  | (8, 6)  | (9, 6)  | (10, 6)  |
| (1, 5)  | (2, 5)  | (3, 5)  | (4, 5)  | (5, 5)  | (6, 5)  | (7, 5)  | (8, 5)  | (9, 5)  | (10, 5)  |
| (1, 4)  | (2, 4)  | (3, 4)  | (4, 4)  | (5, 4)  | (6, 4)  | (7, 4)  | (8, 4)  | (9, 4)  | (10, 4)  |
| (1, 3)  | (2, 3)  | (3, 3)  | (4, 3)  | (5, 3)  | (6, 3)  | (7, 3)  | (8, 3)  | (9, 3)  | (10, 3)  |
| (1, 2)  | (2, 2)  | (3, 2)  | (4, 2)  | (5, 2)  | (6, 2)  | (7, 2)  | (8, 2)  | (9, 2)  | (10, 2)  |
| (1, 1)  | (2, 1)  | (3, 1)  | (4, 1)  | (5, 1)  | (6, 1)  | (7, 1)  | (8, 1)  | (9, 1)  | (10, 1)  |

Figure 3.3: Projection Plane Example

Each cell is assigned a value in the field and in the realistic scenario, the projection resolution is $100 \times 100$ as it will be shown in the next chapter. For the actual fracture plane, the cell arrangement is identical as shown in Figure 3.3, with each cell having a unique index $i$ that represent its position within the plane. In order to extract the value from projection plane to the fracture plane, the following calculations are used:

$$x_{index} = x_{resolution} * \alpha, \tag{3.1}$$

$$y_{index} = y_{resolution} * \beta. \tag{3.2}$$

The two equations above find the cell index in projection plane from the normalized coordinate $\alpha$ and $\beta$. If either of the index is smaller than zero, set it to be equal to zero. On the other hand, if the index exceeds the resolution range, set it equal to the resolution value. These behaviors are usually caused by rounding errors.

Finally, the value of cell index i within the fracture plane is assigned with the following expression

$$\text{Fracture Plane}[i] = \text{Projection Plane}[x_{index}][y_{index}]. \tag{3.3}$$

## 3.4. Fracture Aperture Distribution

The heterogeneity of fault plane depends on sampling algorithms. In this section, the type of sampling method introduced is the power law power spectrum model. The code is generated from "FyeldGenerator" package on GitHub (GitHub, 2018). Parameters to produce reasonable aperture distribution include standard deviation, mean, shape of the field and the seed.

The field length scale depends on the dimension of the projected fracture plane. For example, in Figure 3.1, the width of the plane is 1000 m and the height is 1420 m, which means the ratio of height to width is 1.5, and this value can be applied for the length scale vector. Furthermore, the seed number is a random integer number that produces a unique distribution, and it can be altered for ensemble simulations.

The initial distribution represents the fracture aperture. In order to obtain permeability distribution within the fracture plane, which is assumed to be ranging from $10^5$ to $10^7$ mD, the following calculation is

carried out:

$$k = S * \frac{(\frac{h}{10^3})^2}{12} * 10^{15} \tag{3.4}$$

In equation 3.4, $k$ is permeability, $h$ is fracture aperture width, and $S$ is a scale factor applied to achieved the desired permeability value range. In this case, $S = 3$ is chosen.

Also, for the power-law distribution, the mesh grid is first set up in the Fourier space by applying discrete Fourier transform with available python functions "numpy.fft.fft" and return the sample frequencies with function "numpy.fft.fftfreq" depending on the field size. Two sets of data are sampled from a normal distribution with determined mean, standard deviation and field shape. The first set of data serves as the real part of output, while the other set is the imaginary part. The norm is calculated at each point within the grid and the Fourier field is applied with a multiplier matrix with the definition shown as below:

$$\text{Multiplier} = \begin{cases} 0 & \text{if Norm = 0} \\ (\text{Norm}^n)^{1/2} & \text{if Otherwise} \end{cases}, \tag{3.5}$$

where $n$ is the power of the function, and it is arbitrarily determined based on the desired distribution outcome.

All relevant parameters to set up the distribution mentioned above are summarized in the table 3.1.

| Parameter | Value |
|---|---|
| Mean | 0.001 |
| Standard Deviation | 0.4 |
| Field Size | 300 (Y) by 200 (X) |
| Seed | 20501 |

Table 3.1: Power Law Normal Distribution Parameters

An example of the power spectrum normal distribution for fracture aperture on the initial 2D plane and its projected fracture plane is shown in Figure 3.4.



(a) Projection Plane
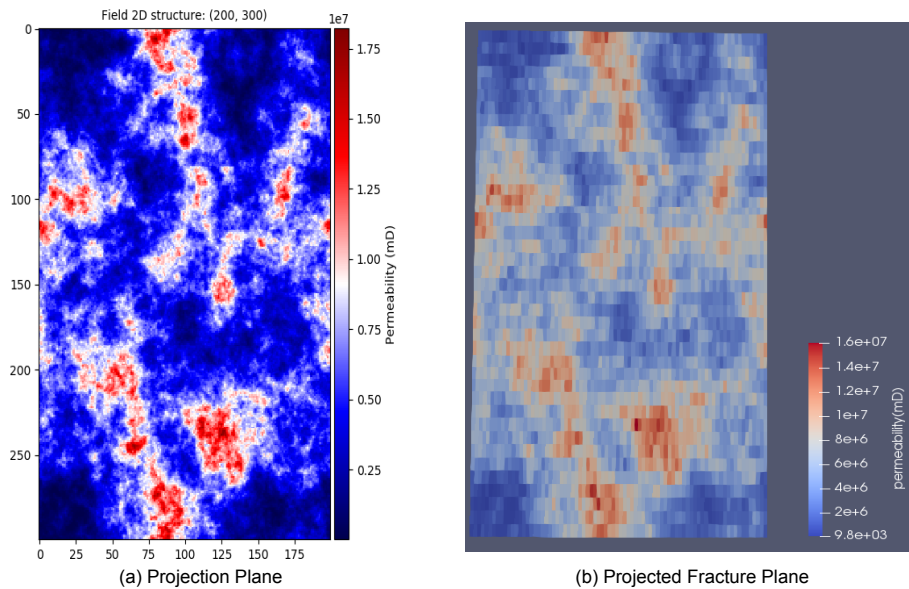
(b) Projected Fracture Plane

Figure 3.4: Permeability Power Spectrum Normal Distribution on Projection Plane (Left) and Projected Fracture Plane (Right)

Note that the distribution above shown has more variability for permeability, which justifies it for being a reasonable representation of fault aperture as within the fault zone difference features such a deformation band and joints can have discrepancies up to 6 orders of magnitude (Flodin, 2002).

4

# Model and Numerical Convergence

## 4.1. Model Set-Up and Parameter Determination

The model layout as well as the well position for all tested resolution cases is displayed in the Figure 4.1. The injection well is represented by the blue cylinder, while the production well is yellow cylinder. Although the wells are shown as drilled at an angle throughout the entire model in this figure, it is solely for the purpose of illustration. Realistically, the wells are drilled vertically first and then slight deviate at the angle of fracture plane to optimize production from the perforation zone. Thus, Figure 4.1 only shows the potential perforations within the reservoir, and the specific location and number of perforations can be set up to satisfy proper simulation conditions.

For simulations and sensitivity analysis, the perforation zone is assumed to be only at the bottom layer which corresponds to the granitic reservoir. The height of the perforated zone is 125 m in the middle to top part of the granitic layer. The total thickness of model is 1620 m including the over-burden and under-burden layer, which is both assumed to be 100 m.
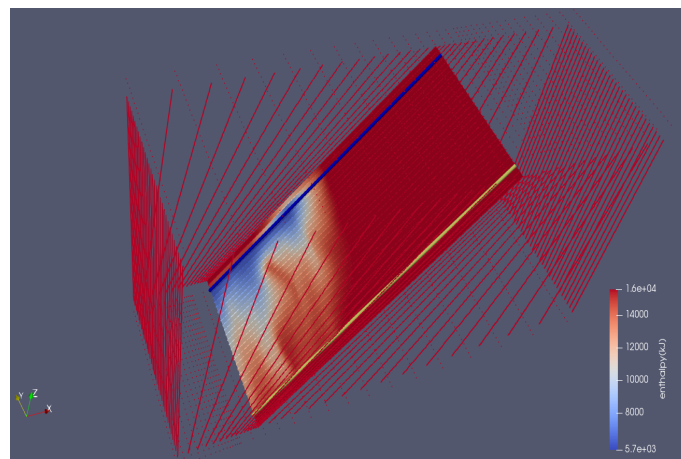


Figure 4.1: Simulation Model Set-Up for Resolution Test

In order to observe the impact of different grid resolution on the results and determine the optimal resolution for ensemble simulations, a series of test is performed with various cell size in x, y and z direction. The permeability or aperture pressure dependence is not accounted for in this case.

The resolution tested are 10, 20, 40 and 80 for x, y and z direction independently. With each set of resolution, x and y resolution remains identical to each other while z resolution changes with the designated values. As the injection rate and production pressure is controlled, the primary results for reference

are production temperature and simulation time. For the consequent ensemble runs, other parameters such as energy production and Net Present Value (NPV) will be taken into consideration as well.

One crucial parameter that alters with changing resolution is the well index, and its calculation is displayed In Equation 4.1 (Eclipse, 2008).

$$WI = \frac{C \Delta z}{ln(\frac{r_o}{r_w})}, \tag{4.1}$$

where $C$ is a constant to be applied in the Peaceman's formula for elongated grids, $r_w$ is the well radius and $r_o$ is the pressure equivalent radius from the grid block, which is defined as below (Eclipse, 2008):

$$r_o = 0.28 * \frac{(D_x{}^2 (\frac{K_y}{K_x})^{\frac{1}{2}} + D_y{}^2 (\frac{K_x}{K_y})^{\frac{1}{2}})^{\frac{1}{2}}}{(\frac{K_y}{K_x})^{\frac{1}{4}} + (\frac{K_x}{K_y})^{\frac{1}{4}}}. \tag{4.2}$$

For simplicity, the permeability is assumed to be isotropic and the x dimension of block $D_x$ is negligible since the fracture plane lays in y-z plane and the fracture width that exists in x direction is several orders of magnitude smaller than the y and z dimensions. Therefore, $r_o$ can be estimated to be equal to $0.2D_y$.

The simulation condition is specified in the table below. For Rittershoffen field, the average production rate is at 280 m$^3$ per hour with 96 % availability (Ravier, 2020), which means each day the water flow volume is 6500 m$^3$. However, as it is mentioned previously, the perforation zone for the simulation model is around 125 m, yet for the Rittershoffen field the average perforation zone is over 500 m in average for the well doublet as shown by the scheme below (Baujard, 2016).
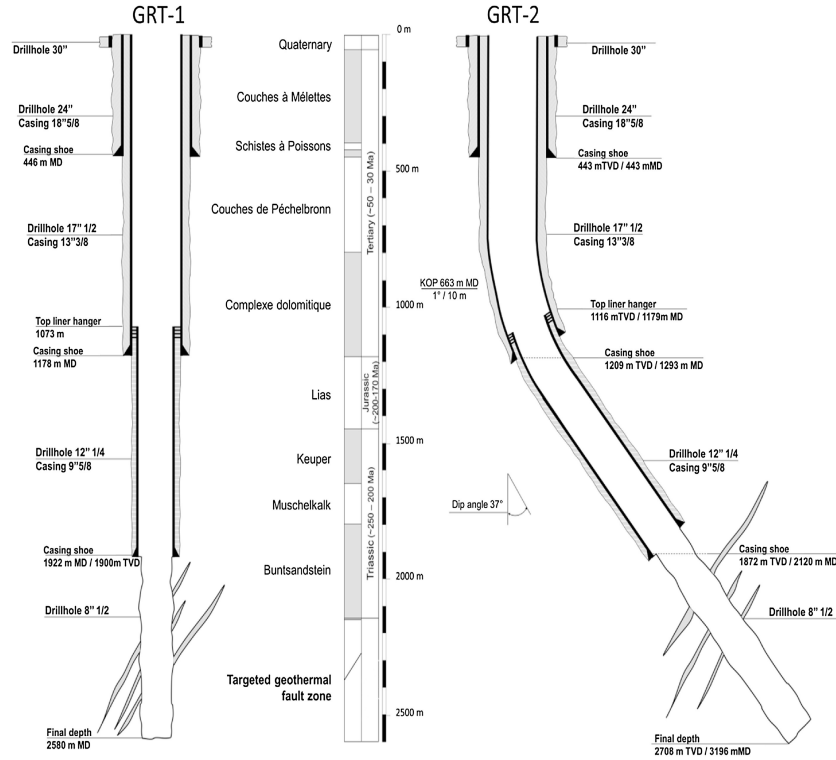


Figure 4.2: Rittershoffen Geothermal Well Couplet Trajectories

Therefore, the injection rate also needs to be scaled down to avoid over-pressuring the reservoir, which means the injection rate for all simulation cases is set at 1000 m$^3$ per day for reasonable outcomes.

The injection temperature can also be referenced from the interference tests of the two geothermal fields as well as Table 1.1. For both Rittershoffen and Soultz-sous-Forets, the inject temperature range

from 70 to 80 °C and the production temperature is within the range of 160 to 170 °C (Portier et al, 2018) (Moucho et al, 2018). Therefore, the injection temperature is set at 70 °C for all cases. The rest of the parameters are taken from the introduction chapter and they are summarized in the table 4.1.

| Parameter | Value |
|---|---|
| Reservoir Initial Temperature, K | 473.15 |
| Reservoir Initial Pressure, Bar | 250 |
| Injection Rate, m3/D | 1000 |
| Injection Temperature, K | 343.15 |
| Production BHP, Bar | 200 |
| Simulation Total Time, Days | 20000 |

Table 4.1: Simulation Conditions

Note that these are the parameters for the base case ensemble simulations. For the sensitivity analysis with other cases, some parameters will vary.

## 4.2. Numerical Convergence Analysis

The simulation time for each chosen resolution mentioned in the previous section will be tested to observe the trend. The convergence test is mainly done on the production temperature to see at which resolution the results start to numerically converge.

### 4.2.1. Homogeneous Case

For homogeneous case, the permeability within the fracture plane is assumed to be uniformly distributed at $k = 10^7$ mD. The simulation time for each resolution is recorded in the table 4.2 and the follow up figures.

| Resolution | Initialization Time | Simulation Time | Total Elapsed Time |
|---|---|---|---|
| 10 * 10 * 10 | 3 | 12 | 15 |
| 10 * 10 * 20 | 4 | 13 | 17 |
| 10 * 10 * 40 | 10 | 17 | 27 |
| 10 * 10 * 80 | 22 | 22 | 44 |
| 20 * 20 * 10 | 9 | 21 | 30 |
| 20 * 20 * 20 | 19 | 32 | 51 |
| 20 * 20 * 40 | 53 | 57 | 110 |
| 20 * 20 * 80 | 120 | 87 | 207 |
| 40 * 40 * 10 | 42 | 50 | 92 |
| 40 * 40 * 20 | 95 | 83 | 178 |
| 40 * 40 * 40 | 269 | 185 | 454 |
| 40 * 40 * 80 | 793 | 415 | 1208 |
| 80 * 80 * 10 | 211 | 254 | 465 |
| 80 * 80 * 20 | 530 | 477 | 1007 |
| 80 * 80 * 40 | 1567 | 1120 | 2687 |
| 80 * 80 * 80 | 4806 | 2203 | 7009 |

Table 4.2: Simulation Time for Tested Resolutions - Homogeneous Case

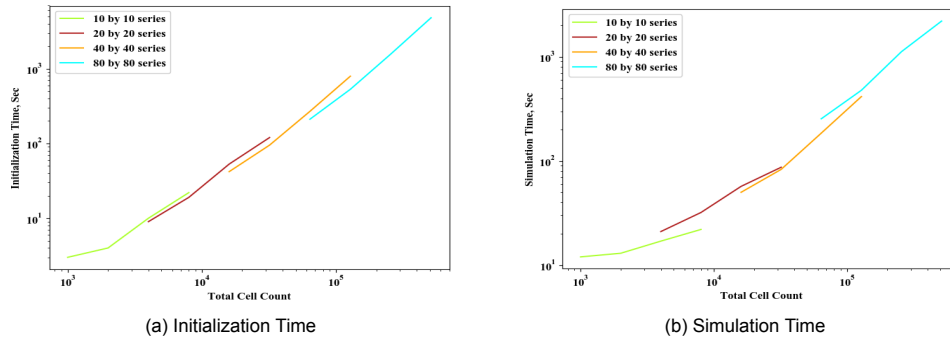(a) Initialization Time

(b) Simulation Time

Figure 4.3: Initialization and Simulation Time for Resolutions Chosen - Homogeneous Case
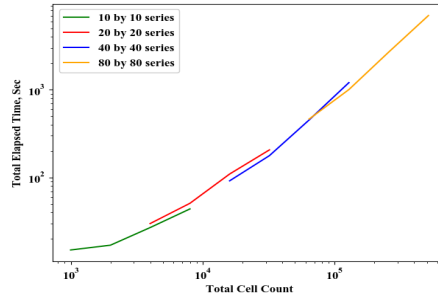
8



Figure 4.4: Total Elapsed Time for Tested Resolutions - Homogeneous Case

The production temperature for tested resolutions is shown in the plot below:
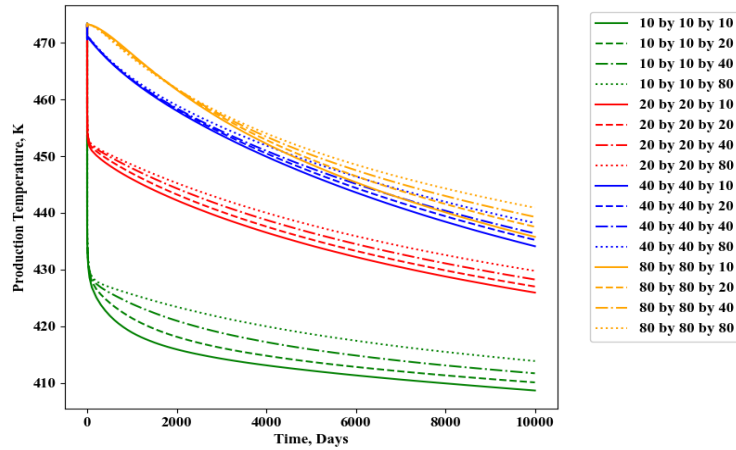


Figure 4.5: Temperature Variation of Different Resolutions - Homogeneous Case

For better observation of the trend in the figure above, the difference between end temperature result from each resolution and the highest resolution applied (in this case, $80 \times 80 \times 80$) are calculated. The plot is shown as below.
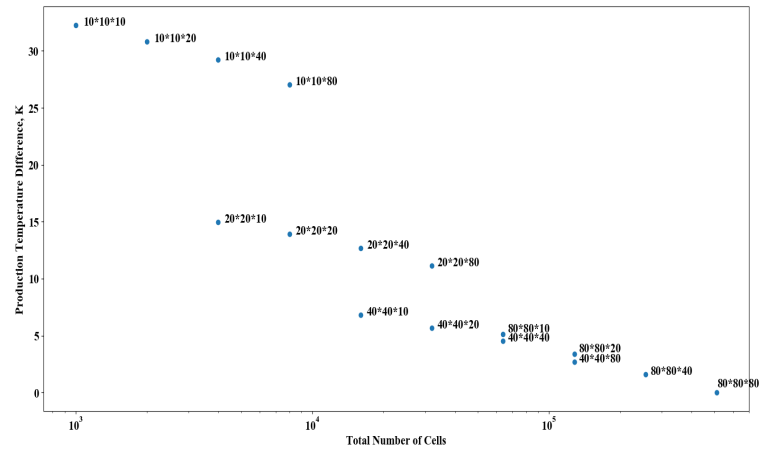
Figure 4.6: End Temperature Difference Among Resolutions with Reference to Highest Resolution Applied

## 4.2.2. Heterogeneous Case

For heterogeneous case, the fracture aperture distribution introduced in Chapter 3 is applied with the same seed number throughout the test. The simulation time for each resolution is recorded in the table 4.3 and the follow up figures.

| Resolution | Initialization Time | Simulation Time | Total Elapsed Time |
|---|---|---|---|
| 10 * 10 * 10 | 2 | 21 | 23 |
| 10 * 10 * 20 | 5 | 25 | 30 |
| 10 * 10 * 40 | 10 | 29 | 39 |
| 10 * 10 * 80 | 21 | 35 | 56 |
| 20 * 20 * 10 | 10 | 47 | 57 |
| 20 * 20 * 20 | 22 | 58 | 80 |
| 20 * 20 * 40 | 52 | 89 | 141 |
| 20 * 20 * 80 | 147 | 129 | 276 |
| 40 * 40 * 10 | 50 | 95 | 145 |
| 40 * 40 * 20 | 119 | 126 | 245 |
| 40 * 40 * 40 | 269 | 218 | 487 |
| 40 * 40 * 80 | 790 | 437 | 1227 |
| 80 * 80 * 10 | 229 | 304 | 533 |
| 80 * 80 * 20 | 579 | 521 | 1100 |
| 80 * 80 * 40 | 1411 | 917 | 2328 |
| 80 * 80 * 80 | 4865 | 1910 | 6775 |

Table 4.3: Simulation Time for Tested Resolutions - Heterogeneous Case



(a) Initialization Time
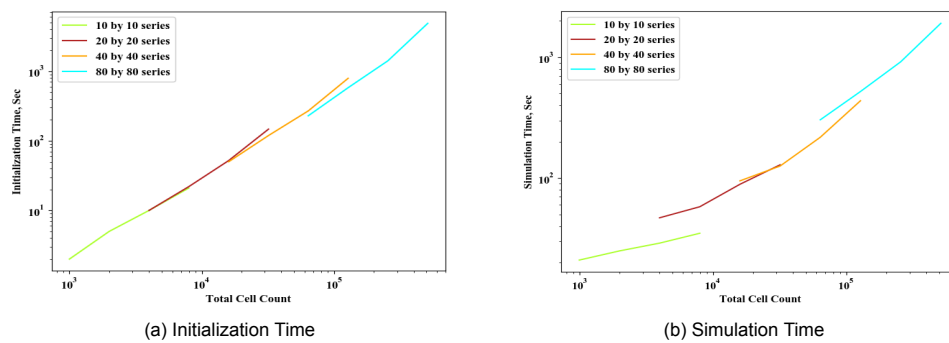


(b) Simulation Time

Figure 4.7: Initialization and Simulation Time for Resolutions Chosen - Heterogeneous Case
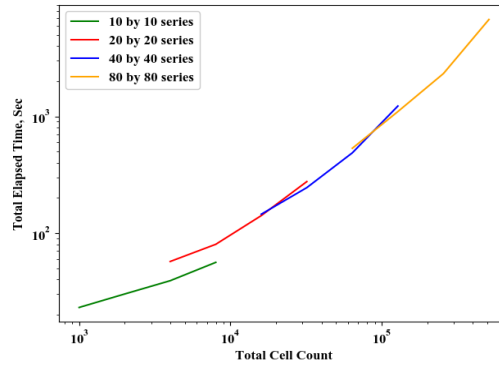
Figure 4.8: Total Elapsed Time for Tested Resolutions - Heterogeneous Case

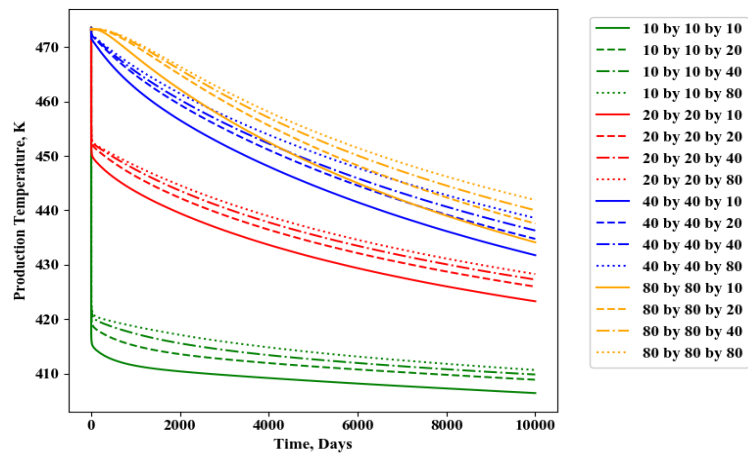The production temperature results for tested resolutions is shown in the plots below:



Figure 4.9: Temperature Variation of Different Resolutions - Heterogeneous Case

The temperature result discrepancies in relative to the results of highest resolution applied is shown in the figure below.
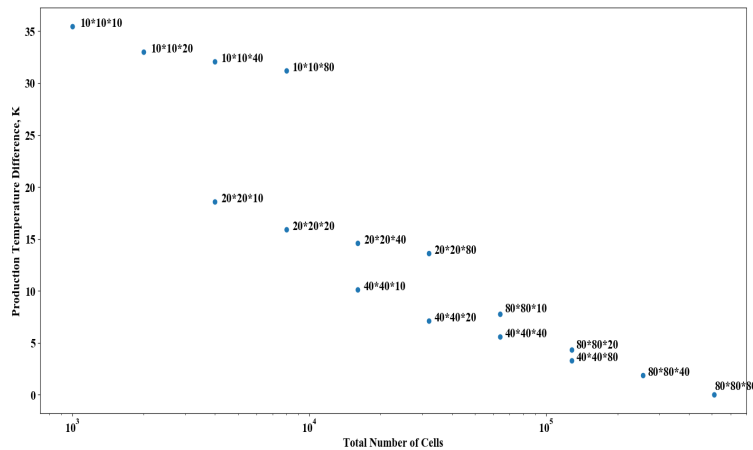


Figure 4.10: End Temperature Difference Among Resolutions with Reference to Highest Resolution Applied

As it can be observed in Figures 4.3, 4.4, 4.7 and 4.8, simulation time generally increases with finer resolution and greater amount of cells. All 6 plots are plotted on log-log scale and the presence of adequate linearity in the lines indicates possible power relationship between cell count and running time. It

is worth noting that some resolution has equal amount of cells, for example between $40 \times 40 \times 20$ and $20 \times 20 \times 80$, yet the latter resolution takes more time to run that the former one. This is most likely due to the fact that the resolution within the fracture plane, which lays in y-z plane, is much greater in $20 \times 20 \times 80$ than $40 \times 40 \times 20$. With more fault cells present, the calculation time is also greater for matrix-fracture as well as fracture-fracture, where most of the energy and mass dynamic occur.

Furthermore, the resemblance of the plot shape between total elapsed time and initialization time indicates that mesh initialization takes up the majority portion of the running time and should be focused when it comes to ensemble simulation as well as optimization.

From the end production temperature error plot Figure 4.6 and Figure 4.10, it can be observed that within the same x and y resolution group, the error declines with the increase of z resolution, which is as expected because a higher z resolution represents more accurate depiction of flow behavior within the fracture. Between different x and y resolution group, some sets of resolution have the same number of cells (e.x. $20 \times 20 \times 40$ and $40 \times 40 \times 10$). For x and y resolution group $20 \times 20$ and $40 \times 40$, the reduction in production temperature solely depends on the resolution in x and y direction no matter what the z resolution is. The opposite trend is observed in x and y resolution group $40 \times 40$ and $80 \times 80$, in which if two set of resolutions have the same amount of cells, the set with greater z resolution demonstrates a smaller errors as it evidently shows in Figure 4.6 and 4.10. Thus, a suitable resolution for ensemble simulations should be chosen from x and y resolution group of $80 \times 80$ due to the diminishing impact on the results from resolutions in x and y direction. By taking account of the error margin and simulation time, the final resolution to be applied is $80 \times 80 \times 40$, whose end production temperature is no more than 1.5 degrees different from the highest resolution result for both homogeneous and heterogeneous cases.

## 4.3. Net Present Value Model

The purpose of NPV model is to evaluate the financial outcome of each realization to observe the impact of certain input parameters on the project lifetime. Relevant items in the model include capital cost, operation cost (pumping and power usage), tax and interest rate, and energy revenue from heat production. Due to the lack of financial data from Rittershoffen project, many parameters introduced below will be obtained from European renewable energy regulations and policies as well as previous or existing Dutch geothermal projects.

### 4.3.1. Discount, Royalty and Tax Rate

The Financial Incentive Guideline (FIG) aims to encourage the development of geothermal reservoirs with minimum financial burden. This means minimum license fee and a royalty rate of 0 % (Geothermal Regulation Framework, 2009). Although there is no detailed info on the tax rate for Rittershoffen or Soultz-sou-Forets project, the Dutch corporate tax rate of 25 % can be applied (Rijksoverheid, 2020). The overall discount rate is determined through the weight average cost of capital, which is also known as WACC. The WACC rate can also be considered as the minimum required interest rate of a project, which is important in determine the economic viability of the investment. The expression of WACC is shown as below (Investopedia, 2019):

$$WACC = \frac{E}{V} * R_e + \frac{D}{V} * R_d * (1 - T_c) \tag{4.3}$$

In the equation above, E and D represents equity market value and debt market value, and V stands for total market value of the project, which is summation of E and D. A typical D/E ratio is 70/30 in the Netherlands (Zaal, 2020). Furthermore, $R_e$ is cost of equity and $R_d$ us cost of debt. For geothermal projects, $R_e$ is 14.5 % and $R_d$ is 2 % (van der Welle, 2018). Last but not least, $T_c$ is the corporate tax rate, which is set at 25 % as it has been mentioned above.

With the provided equation and values, the WACC rate is calculated to be 5.4 % on a yearly basis, which will be applied as the discount rate in this NPV model.

Since the simulation does not have equal time steps of 365 days, it is important to convert the discount rate with the actual time period with the following equation (Investopedia, 2020):

$$\text{Periodic Rate} = (1 + r)^{t/T} - 1, \tag{4.4}$$

where $r$ represents discount rate over the nominal period, $t$ is the actual period and $T$ is the nominal period.

### 4.3.2. Capital Expense
The main capital expense (CapEx) considered for the NPV model are well cost and equipment expenditure. All capital expense is assumed to incur in the first year. The well cost includes the facility installation cost and it also depends on the drilling depth as the following equation shows (ThermoGIS, 2020):

$$Well_{CapEx} = 375000 + 1150 * depth + 0.3 * depth^2 \tag{4.5}$$

The depth of drilling is 2500 m for both injector and producer as shown by Figure 4.2. Thus, the total well costs come up to be 10.25 million Euros.

The second portion of the capital expense, the equipment expenditure, sums up the cost of injection pump, electric submersible pump, the heat exchanger and other relevant facilities. While the electric submersible pump costs up to 800,000 Euros (Daniilidis, 2017), the rest of the equipment can cost up to 1.5 million Euros (Kasalsenergiebron, 2013), and this adds to a total equipment expenditure of 2.3 million Euros.

### 4.3.3. Operational Expense
The operational expense (OpEx) represents all expenditures during the production period such as electricity consumption and staff cost. There are two categories of operational expense, namely variable OpEx and fixed OpEx. For simplicity, the variable OpEx considered in this model only includes the electricity usage from the pump. A recent study uses two years of deep geothermal project operation experience in Upper Rhine Graben to conclude that operational cost, which includes auxiliary consumption such as chemical treatment and electricity usage, is estimated to be around 2.5 to 3 % of capital cost each year (Mouchot et al, 2019). Thus, for the NPV model, a fixed rate of operational cost will be set at 2.5 % of CAPEX.

For the variable OpEx, the pumping energy is calculated as the summation of injection and production pumping energy. For each of these two categories, as Equation 4.6, the pumping energy is dependent on the pressure difference between bottom hole pressure and reservoir pressure as well as injected or produced water rate (Neutrium, 2020). The price value of 0.094 Euro per kWh is determined through the latest data available for Dutch industry electricity price (Statista, 2020).

$$\text{Pumping Energy} = \frac{Q \Delta P}{3600} * 60 * 60 * 24 \tag{4.6}$$

In Equation 4.6 above, flow rate is in $m^3$/hr, pressure difference is in kPa and the energy unit is KJ.

The efficiency for pumping energy is obtained from the overall efficiency of an ESP pump, which is typically in the range of 55 % (Spijker & Ungemach, 2016).

### 4.3.4. Energy Production Revenue
The produced heat needs to convert to electricity energy for commercial purpose. From the recent study, the average conversion efficiency of geothermal plants is 12 % (Sadiq et al, 2014). The sale price of electricity is commonly less than that of the price for electricity consumption for geothermal projects. Due to lack of data, it is assumed the electricity sale price is 75 % of the consumption price, which is calculated to be 0.070 Euro per kWh. The electricity price is assumed to be constant throughout the project life and any subsidy scheme is not taken into consideration in this NPV model.

### 4.3.5. Parameters Summary

All economic parameters mentioned above are summarized in the table below.

| Parameter | Value |
| --- | --- |
| Capital Expense - Wells, million Euros | 10.25 |
| Capital Expense - Equipment, million Euros | 2.3 |
| Operational Expense - Fixed , million Euros / Year | 0.025 * CAPEX |
| Operational Expense - Variable , million Euros / Year | See Equation 4.6 |
| Tax Rate, % | 25 |
| Discount Rate (WACC), % | 5.4 |
| Heat to Electricity Conversion Efficiency, % | 12 |
| Pump Efficiency, % | 55 |
| Electricity Usage Price, Euro / kWh | 0.094 |
| Electricity Revenue Price, Euro / kWh | 0.070 |
| Project Life, Days | 20000 |

Table 4.4: NPV Model Parameters

An example NPV curve is shown as below, note how the line starts to flatten out near the end of project life due to the compounding effect of discount rate.
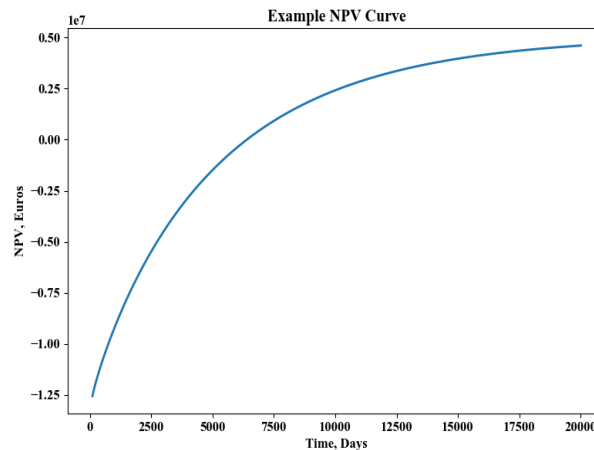


Figure 4.11: NPV Example Curve

An example of NPV workflow is attached in the appendix listing all the components of the model.

# 5

# Simulation Results and Discussion

Next we investigate the impact of fracture aperture or permeability distribution on the outcome of parameters of interest. The chosen resolution is $80 \times 80 \times 40$ for all scenarios and 100 realizations are executed. For every realization, a different seed number is assigned to the appropriate distribution function while the mean and standard deviation remain identical. For sensitivity analysis with other scenarios, the same 100 aperture distributions are applied.

## 5.1. Base Case

For base case, the well couplet is placed at 850 m from each other and the pressure-permeability dependence is expressed by non-linear correlation as shown by Equation 2.14 in previous chapter. A summary of parameters applied is shown in the table below.

| Parameter | Value |
|---|---|
| Reservoir Initial Temperature, K | 473.15 |
| Reservoir Initial Pressure, Bar | 250 |
| Injection Rate, m3/D | 1000 |
| Injection Temperature, K | 343.15 |
| Production BHP, Bar | 200 |
| Well Spacing, m | 850 |
| Permeability/Aperture Pressure-Dependence | see Equation 2.14 |
| Simulation Total Time, Days | 20000 |

Table 5.1: Base Case Simulation Conditions

The results production temperature, pressure difference between injector and producer, net cumulative energy production and NPV for each realization are shown as below.
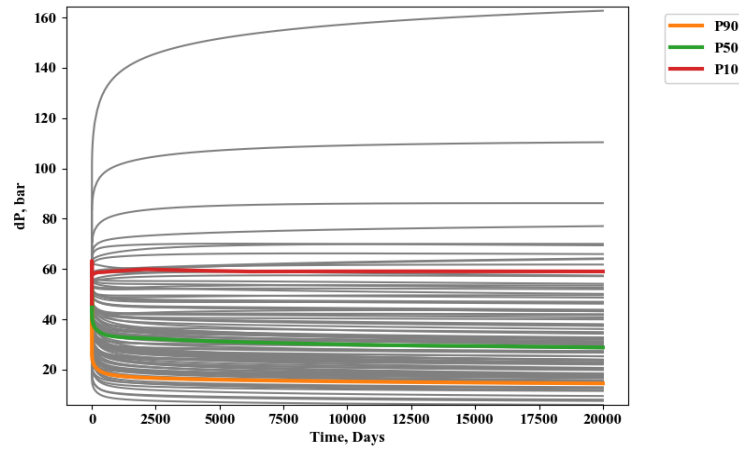
Figure 5.1: Ensemble Simulation Base Case Pressure Difference

Although it goes as high as 160 bar, the pressure difference between injector and producer is mostly under 80 bar. The scale of permeability for power-law normal distribution that is used in this base case is approximately $10^7$ mD, and very few cell's permeability is more than two orders of magnitude smaller than this range. As the production pressure is fixed while injection pressure depends on the perforated cells' permeability, the chance of having a series of low permeability injection cell and the reservoir getting over pressurized is rather low. Therefore, for most realizations, the pressure difference is at a reasonable operational condition.
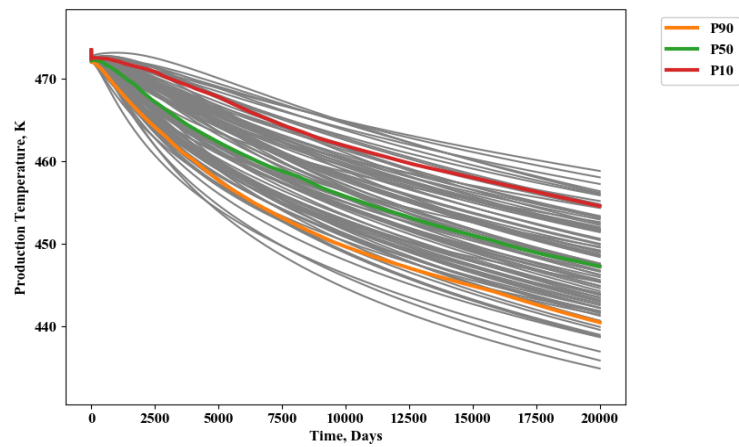


Figure 5.2: Ensemble Simulation Base Case Production Temperature

The variation of end production temperature ranges from 465 to as low as 430 K. This is a crucial parameters as it is an indication of the energy production because the temperature is a function of pressure and enthalpy. As it can be observed in the figure above, while all the other conditions are identical, the difference in permeability distribution within the fracture plane (especially along the flow path between the injector and producer) can greatly impacts the producer temperature, which is an indication of heat extraction. In order to have a better reference of the production temperature with the same temperature drop, the time elapsed to reach 465 K has been displayed in the following histogram.
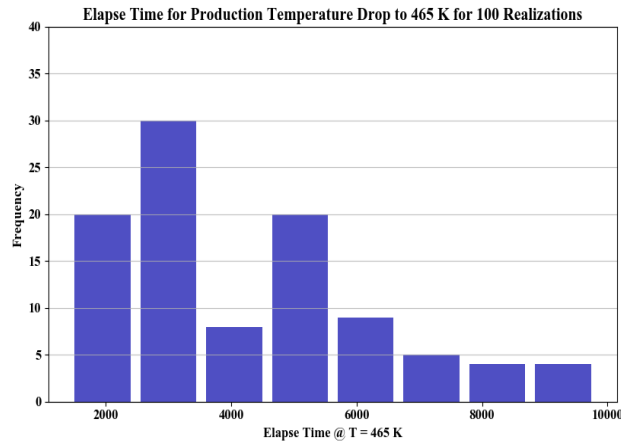
Figure 5.3: Ensemble Simulation Base Case Elapsed Time @ T = 465 K

The average time for the production temperature drops to 465 K is estimated to be 4000 days with very few outliers taking longer than 8000 days.



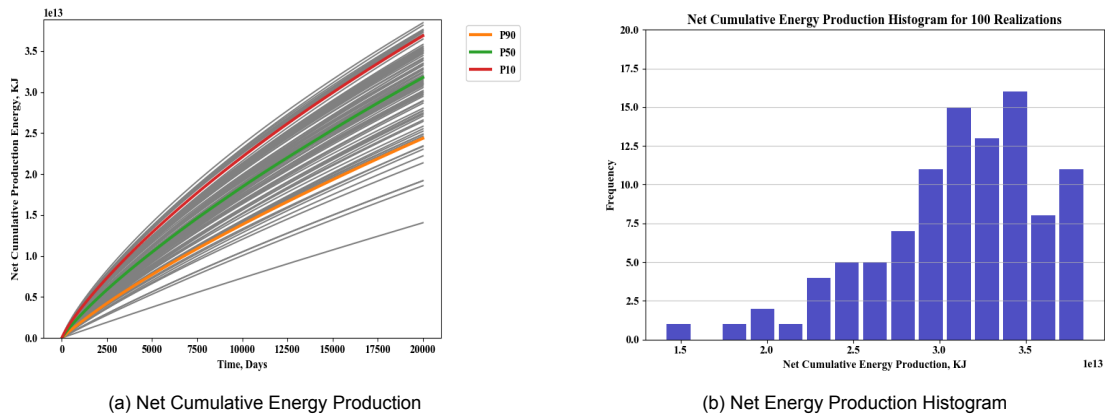(a) Net Cumulative Energy Production                    (b) Net Energy Production Histogram

Figure 5.4: Ensemble Simulation Base Case Net Cumulative Energy Production Results

By taking integral of the energy production rate over time and subtract the pump energy from injector and producer, the cumulative net energy production with declining temperature over simulation time is plotted as below. The range of net energy production is rather large, which goes from 1.5e13 to 3.75e13 KJ as shown in the histogram in Figure 5.4. The large spread of histogram implies that the fracture aperture or permeability distribution in the fracture plane has significant impact on the energy production for geothermal projects.

The histogram for net energy production also displays a close trend to normal distribution with most cases producing from 3.0E13 to 3.5E13 KJ. The shape of the histogram is mostly likely due to the normal sampling process of the fracture aperture power-law distribution.

The net energy production is then translated in the NPV results as shown below with the NPV model parameters discussed in section 5.3.1. Because of the dependency of NPV on net energy production, the shape of histogram for these two parameters are similar as shown by Figure 5.5. NPV results range from -1E7 to 1.4E7 Euros, with most cases in the range of 0.5E7 to 1.0E7 Euros.
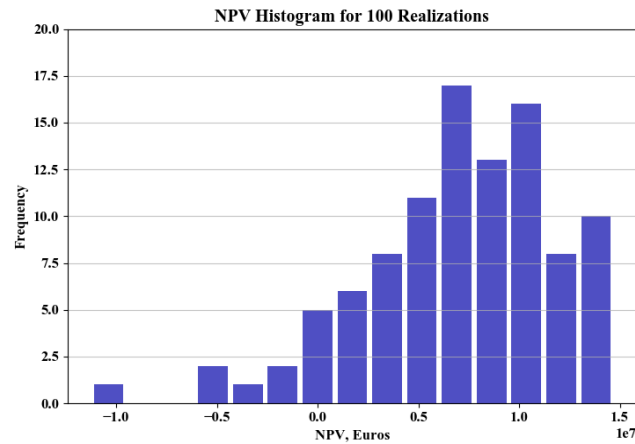
Figure 5.5: Ensemble Simulation Base Case NPV Histogram

A summary of P10, P50 and P90 end results for the variables mentioned above is listed in the table below.

|     | Pressure Difference, Bar | Production Temperature, K | Net Cumulative Energy, KJ | NPV, Euros |
|-----|--------------------------|--------------------------|---------------------------|------------|
| P90 | 14.52                    | 440.52                   | 2.44E13                   | 0.22E6     |
| P50 | 28.83                    | 447.30                   | 3.18E13                   | 7.37E6     |
| P10 | 59.05                    | 454.59                   | 3.69E13                   | 12.60E6    |

Table 5.2: Base Case Results Summary for P10, P50 and P90

## 5.2. Case 1: With No Pressure Dependence

Under the condition of no pressure dependence, the aperture and permeability distribution remains the same throughout the simulation for each realization. The specified conditions are as following:

| Parameter | Value |
|-----------|-------|
| Reservoir Initial Temperature, K | 473.15 |
| Reservoir Initial Pressure, Bar | 250 |
| Injection Rate, m3/D | 1000 |
| Injection Temperature, K | 343.15 |
| Production BHP, Bar | 200 |
| Well Spacing, m | 850 |
| Permeability/Aperture Pressure-Dependence | None |
| Simulation Total Time, Days | 20000 |

Table 5.3: Case with No Pressure Dependence Simulation Conditions
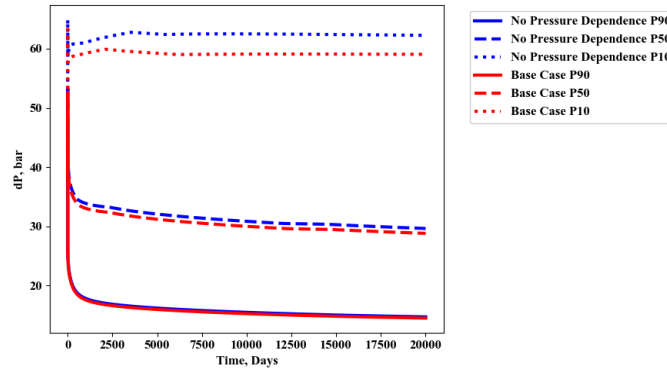
Figure 5.6: Pressure Difference Comparison to Base Case

Without pressure dependence, the injection pressure is slightly higher than that of ensemble runs with nonlinear perm-pressure correlation as shown in Figure 5.6. This trend can be explained by the high injection pressure in the reservoir, which results in an greater increase in aperture or permeability of surrounding blocks for base case with pressure dependence. This in turn reduces the injector pressure as the water is easier to flow through the blocks around injector, which results in a smaller pressure difference between injector and producer as the producer pressure is fixed and it is always less than the injector pressure. For the case with no pressure dependence, the injector pressure builds up faster and creates a greater pressure difference to the producer.
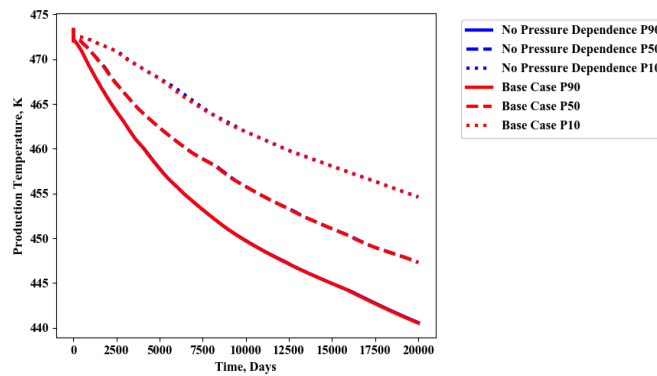


Figure 5.7: Production Temperature Comparison to Base Case

The production temperature trend is nearly identical with the end temperature results vary $\pm$ 0.05 K for P10, P50 and P90. The same behavior can also be observed in the net energy production as shown in Figure 5.9 below, with base case produce only 0.02E13 to 0.03E13 KJ more energy than the no pressure dependence case.

This phenomenon is due to the pressure gradient between injector and producer. As Figure 5.8 shows, although the pressure is high around the injector, it gradually declines as it approaches the producer and pressure of most blocks around the producer does not exceed 210 bar. Refer to Equation 2.14, the minimum pressure is set at 200 bar according to the formation pressure gradient of fresh water in the reservoir, which means that the aperture or permeability of blocks near producer will barely go through any change.

In fact, other than the injector blocks, most blocks in the flow path will not have a drastic increase in the aperture change due to the non-linear pressure dependence log function. Therefore, for the base case only a slight increase in energy production is observed, which is 2 orders of magnitude smaller than the total net energy. Since there is almost no difference in the energy production, it indicates the producer blocks also have very similar enthalpy for both cases, which results in nearly identical production temperature.
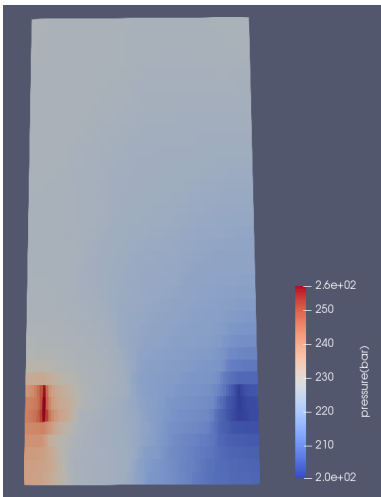
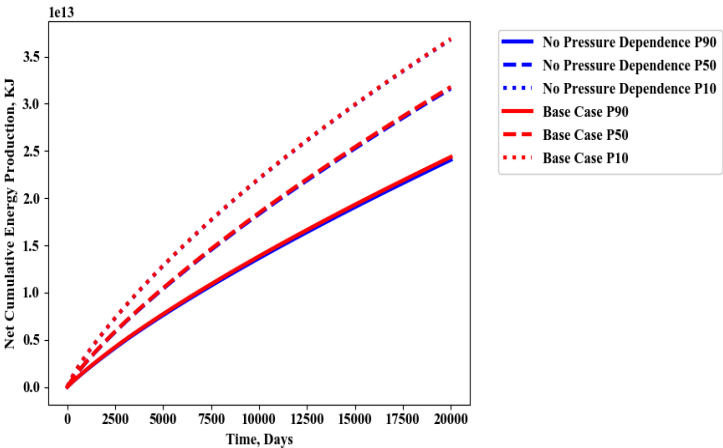Figure 5.8: Pressure Gradient Between Injector and Producer



Figure 5.9: Net Energy Comparison to Base Case

For the reasons stated above, the histogram shape for no pressure dependence case resembles the base case, with values range from 1.5E13 to 3.75E13 KJ.
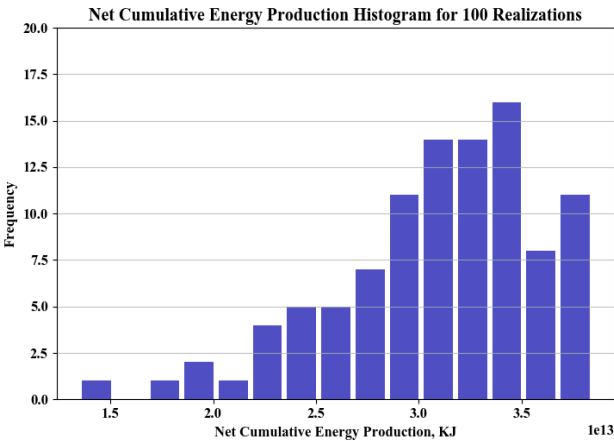


Figure 5.10: Ensemble Simulation Without Pressure Dependence Net Cumulative Energy Production Histogram

The NPV histogram below shows a range of -1.0E7 to 1.40E7 Euros, which is the same range as

the base case. However, despite the identical net energy production and production temperature, the change in pressure difference alters the NPV results and its histogram shape. In this case, a peak frequency is also observed in the range of 0.5E7 to 1.0E7 Euros.
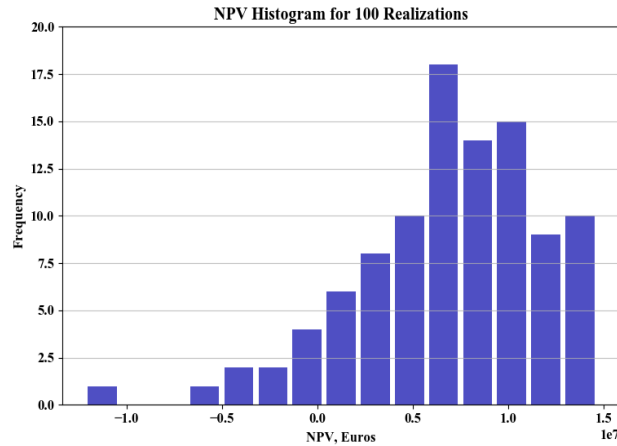


Figure 5.11: Ensemble Simulation Without Pressure Dependence NPV Histogram

## 5.3. Case 2: With Half Distance Between Wells

In this case, both injector and producer well is still in strike direction configuration, but the plane distance between them is reduced to half of base case distance, which is 425 m. Every other condition and parameter stays identical as the base case as Table 5.4 shows below.

| Parameter | Value |
|---|---|
| Reservoir Initial Temperature, K | 473.15 |
| Reservoir Initial Pressure, Bar | 250 |
| Injection Rate, m3/D | 1000 |
| Injection Temperature, K | 343.15 |
| Production BHP, Bar | 200 |
| Well Spacing, m | 425 |
| Permeability/Aperture Pressure-Dependence | see Equation 2.14 |
| Simulation Total Time, Days | 20000 |

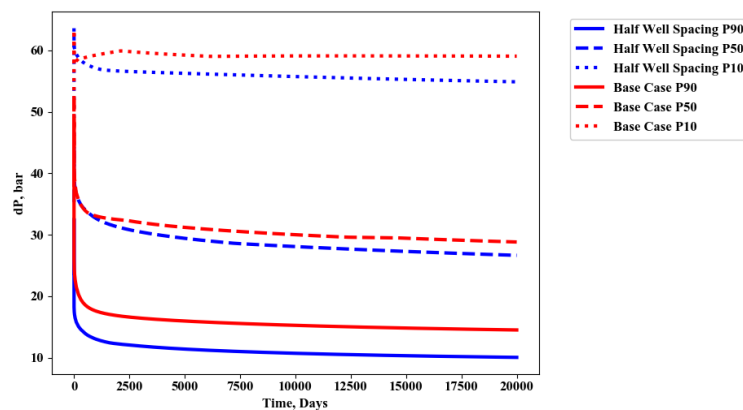Table 5.4: Case with Half Well Spacing Simulation Conditions



Figure 5.12: Pressure Difference Comparison to Base Case

The trend shown in Figure 5.12 is expected because when the injector and producer are closer to each

other, less pressure build up occurs in injector as the injected water now propagates a shorter distance.
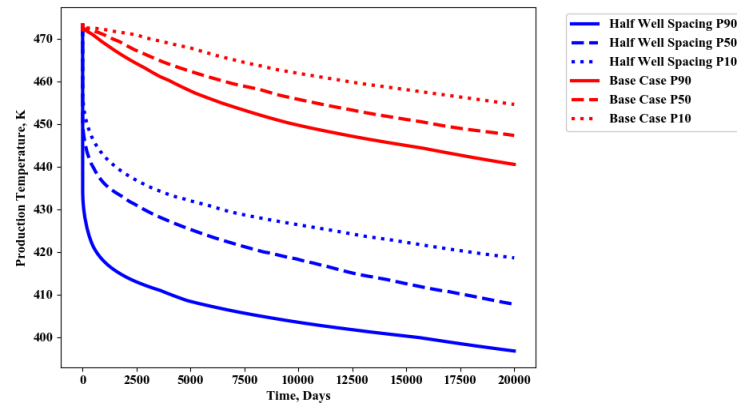


Figure 5.13: Production Temperature Comparison to Base Case
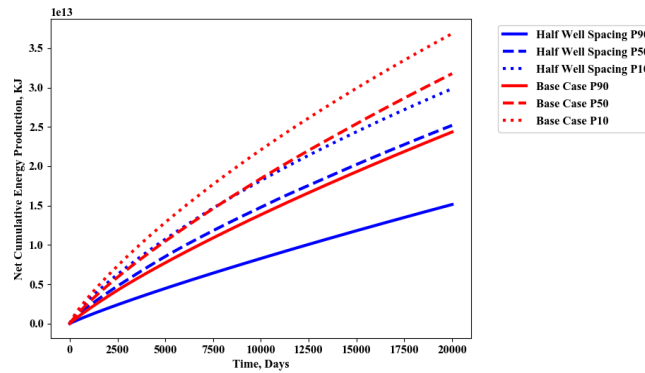


Figure 5.14: Net Energy Comparison to Base Case

As the well spacing is reduced, the injected water flow through less of the reservoir volume and therefore less total amount of energy is extracted at the end of the project life. This also can be reflected in the production temperature for the half well spacing case because the end enthalpy for producer blocks are much lower due to the constant water injection rate yet a lower total enthalpy in the flow path. These trends can be observed in both Figure 5.13 and 5.14 as shown above.



(a) Net Cumulative Energy Production
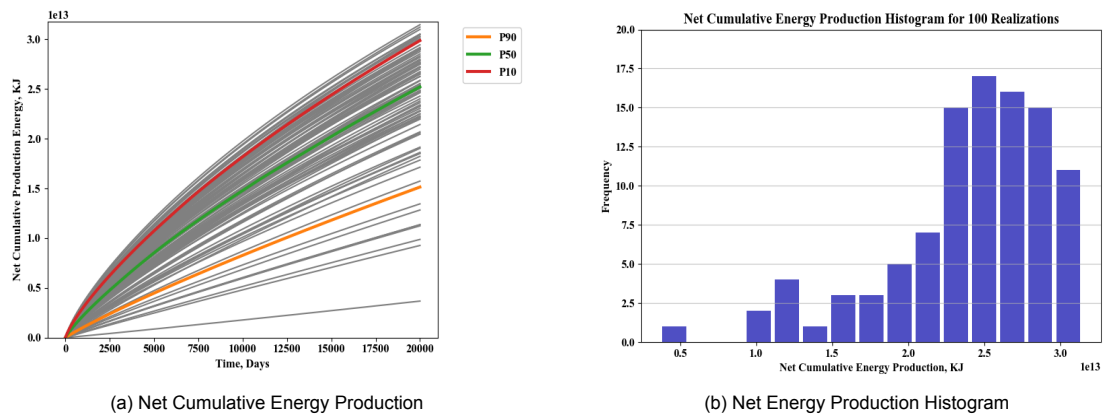
(b) Net Energy Production Histogram

Figure 5.15: Ensemble Simulation Half Well Spacing Net Cumulative Energy Production Results

The total net energy production is much lower than that of the base case for the reasons mentioned above. In Figure 5.15, the histogram indicates the range of net energy production ranges from 1.50E13

to 3.25E13 KJ with the elimination of outliers, and most of the realizations produce from 2.25E13 to 3.00E13 KJ. These ranges numbers are around 1.2 to 3 times smaller than those of the base case.

The NPV result corresponds to the net energy production and it ranges from -1.75E7 to 0.75E7 Euros, with most cases generate -0.25E7 to 0.60E7 Euros. These numbers are approximately half of that of the base case.
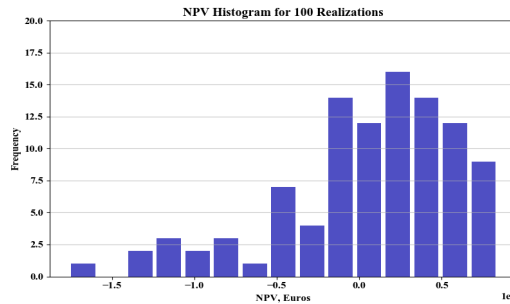


Figure 5.16: Ensemble Simulation Half Well Spacing NPV Histogram

## 5.4. Case 3: Gravity Model with Wells on Strike and Dip Direction

The gravity model takes account of impact of gravity for geothermal productions under the determined conditions. This is especially important when wells are positioned in the dip direction configuration, which is different from the original strike direction configuration in the base case. The impact of implementing gravity module in comparison to a model without gravity is discussed in the Appendix. For both configurations, the fracture plane distance between the injector and producer are both 850 m. For wells in dip direction, the injector is placed at a shallower depth than the producer, which gives a vertical drop of 600 m for the well couplets as the dip angle for the fault is 45 degrees. The set-ups are illustrated in the figure below.



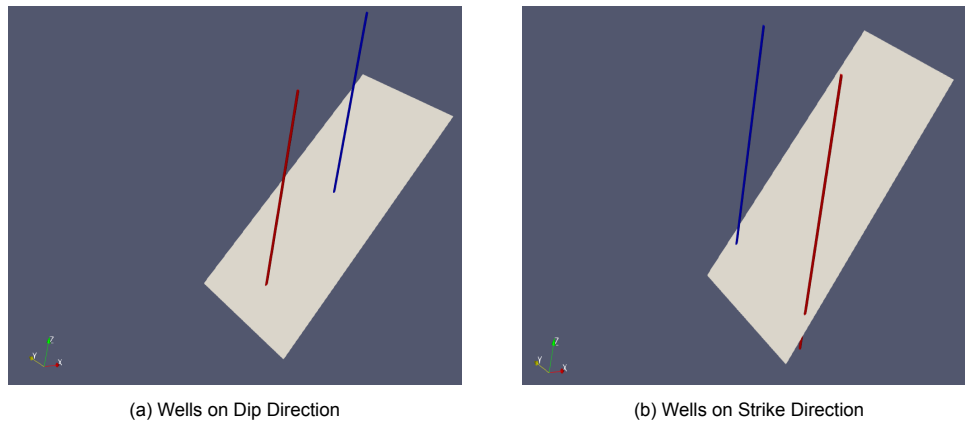(a) Wells on Dip Direction                    (b) Wells on Strike Direction

Figure 5.17: Well Configuration (blue = injector, red = producer)

Another aspect for the gravity model is the alternation of uniform temperature and pressure distribution in the base case. Since the results are depth dependent in the gravity model, temperature and pressure gradient will be applied to create the initial distribution. The temperature gradient refers to the geothermal temperature profile for Rittershoffen project as shown in Figure below (Maurer et al, 2018).
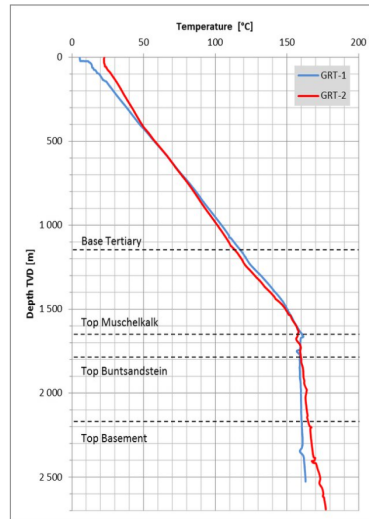
Figure 5.18: Reference Temperature Profile

As it can be observed, for the entire depth of the profile, the average temperature gradient is 0.06 °C per meter.

The pressure gradient is calculated based on the formation pressure gradient with fresh water, which is approximately 0.1 bar per meter.

A summary of simulation condition for the gravity case is listed in the table below.

| Parameter | Value |
|---|---|
| Reservoir Initial Temperature Gradient, deg/m | 0.06 |
| Reservoir Initial Pressure, Bar/m | 0.1 |
| Injection Rate, m3/D | 1000 |
| Injection Temperature, K | 343.15 |
| Production BHP, Bar | 200 |
| Well Spacing (for both Strike and Dip direction), m | 850 |
| Permeability/Aperture Pressure-Dependence | see Equation 2.14 |
| Simulation Total Time, Days | 20000 |

Table 5.5: Case with Gravity Simulation Conditions

With the gradient values specified above, the initial temperature and pressure distribution within the fracture plane model is shown as below.
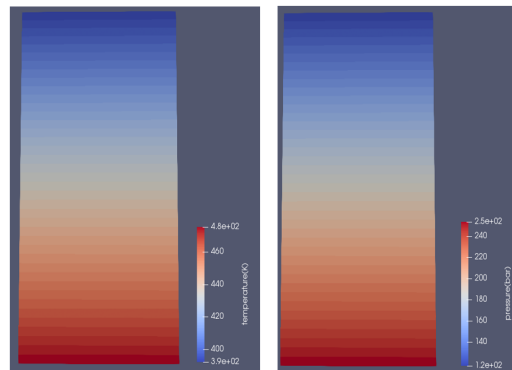


Figure 5.19: Initial Temperature and Pressure Distribution within Fracture Plane

In order to observe the impact of gravity, a test run is performed with same seed of fracture aperture distribution and same conditions shown in table 4.1 except reservoir initial temperature and pressure.
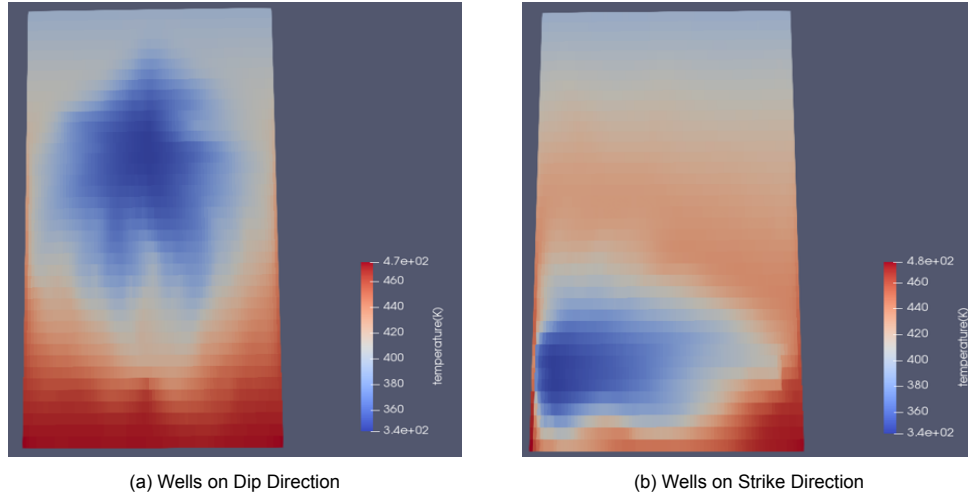


(a) Wells on Dip Direction                                             (b) Wells on Strike Direction

Figure 5.20: Gravity Test Cases Temperature Distribution End Results



(a) Wells on Dip Direction                                             (b) Wells on Strike Direction
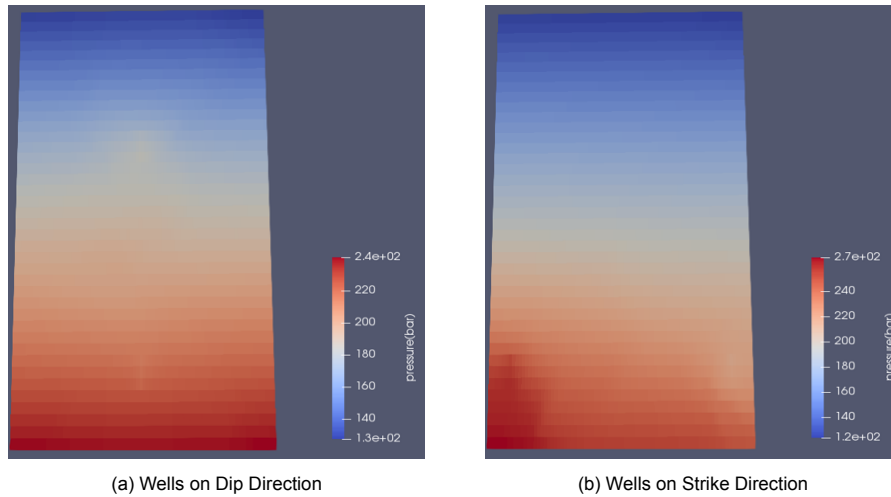
Figure 5.21: Gravity Test Cases Pressure Distribution End Results

The flow path can be observed in Figure 5.20 for two types of well configurations specified, and a low permeable zone is present in the dip direction scenario indicated by the diversion of flow from the temperature pattern. Although the end pressure results has similar distribution with the producer at same depth, the pressure build up at the injector for strike direction placement is much greater than that of the dip direction. This is because of the greater reservoir pressure and potential permeable barrier as indicated by the high pressure zone around the injector in strike placement scenario. Overall, the results above validate the gravity model with the specified conditions.

To better analyze the sensitivity of relevant parameters for the two types of well configurations with the gravity effect, the ensemble simulation of 100 realizations are peformed.

(a) Wells on Dip Direction
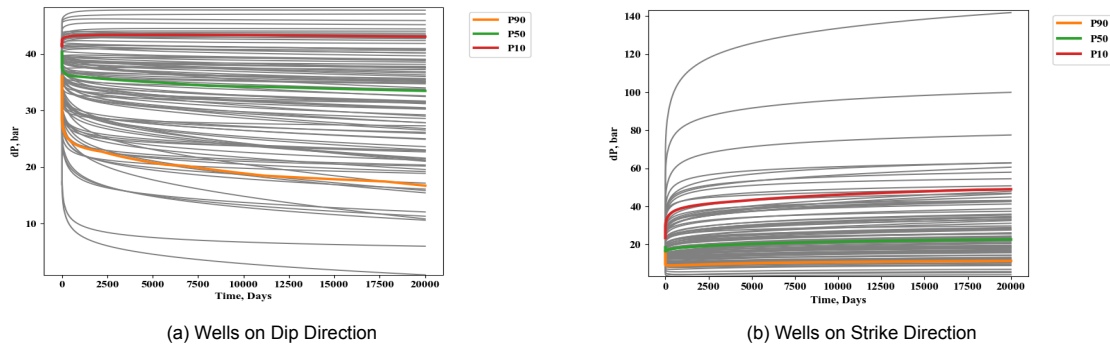
(b) Wells on Strike Direction

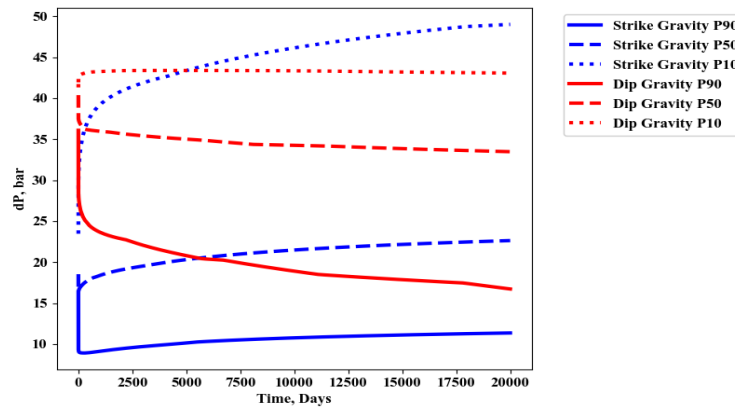Figure 5.22: Gravity Model Ensemble Simulations Pressure Difference Results



Figure 5.23: Gravity Model Ensemble Simulations Pressure Difference Comparison

The pressure difference for dip configuration is generally greater than that of strike configuration as shown in Figure 5.23 because the injector and producer are located at different depth, and therefore the injector pressure is relatively small from the pressure gradient. In Figure 5.22, it can be observed that the pressure difference value is slowly declining for the dip case while it is building up for the strike case from all realizations. The shapes of these curves reflect the impact of gravity-assisted flow, for which in the dip configuration case the flow path between wells is more positively effected by the gravity than the strike configuration case, causing less pressure build-up for the injector and therefore a gradually decreasing pressure difference. More specifically, gravity has a net negative impact for the strike configuration case as it diverts the water flow from its original flow path between the well couplets.



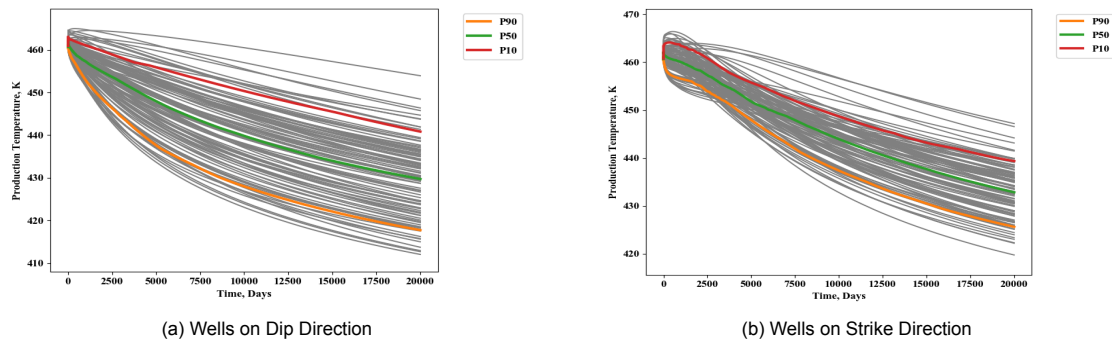(a) Wells on Dip Direction

(b) Wells on Strike Direction

Figure 5.24: Gravity Model Ensemble Simulations Production Temperature Results
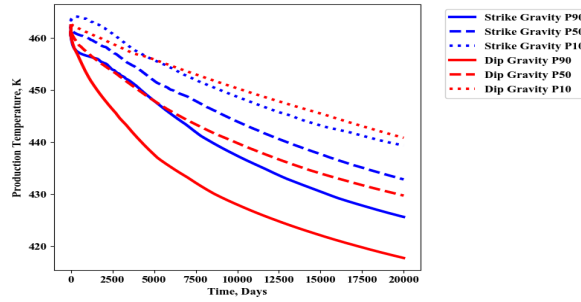
Figure 5.25: Gravity Model Ensemble Simulations Production Temperature Comparison

As Figure 5.25 shows, the production temperature of the dip case is smaller than the strike case. This can be related to the net production energy trend as indicated in Figure 5.27. The comparison for total energy produced between two cases is rather counter-intuitive, as one would expect a greater energy production for the dip direction well configuration because of the gravity assistance. However, a crucial aspect of energy production is the enthalpy in the reservoir volume. With the dip configuration, the flow path between injector and producer has a total net enthalpy that is less than that of the strike case due to the fact that the temperature is smaller at a shallower depth from its gradient, and the enthalpy is a function of temperature as previously mentioned. Thus, it is speculated that the gravity assistance is not sufficient to overweigh the temperature gradient effect on energy production.

As it is stated above, the total enthalpy in the flow path for the dip case is less than the strike case. This means that for the dip case, the water absorbs more heat when it is closer to the production well in comparison to the strike case due to the low heat content of the reservoir cells in the shallower part. This in turn explains the trend that the dip configuration wells have smaller production temperature, which is because the enthalpy close to the producer blocks is depleted faster.



(a) Wells on Dip Direction

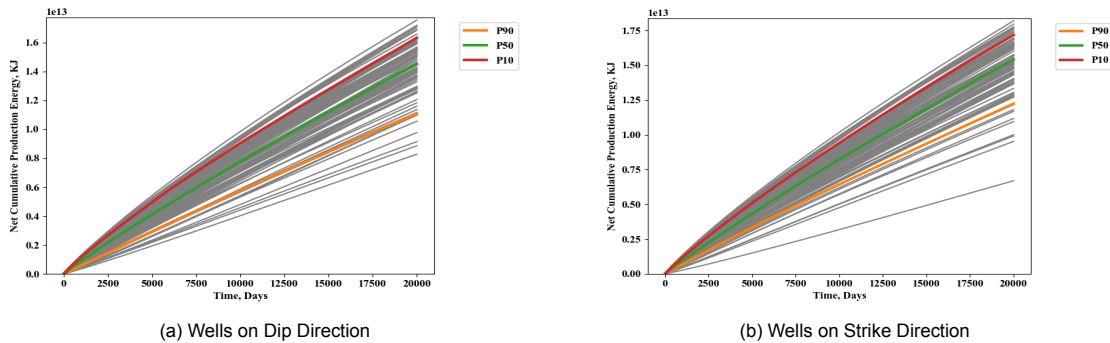(b) Wells on Strike Direction

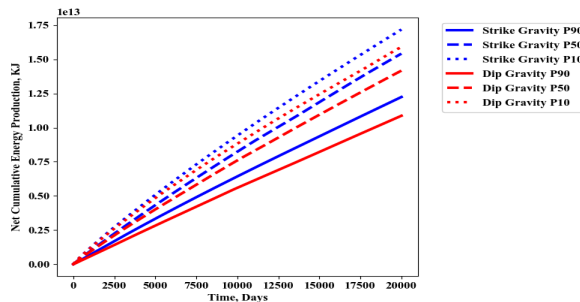Figure 5.26: Gravity Model Ensemble Simulations Net Cumulative Energy Production Results



Figure 5.27: Gravity Model Ensemble Simulations Net Energy Production Comparison

The range for values of net energy production for both well configuration cases is much smaller than that of the base case. There are two reasons for this. The first reason applies to the dip orientation

case, which is the implementation of temperature and pressure distribution based on their gradient instead of the high uniform value distribution in the base case. The second reason applies to the strike orientation case as for the strike configuration, the gravity diverts the water flow from its original path as mentioned above, and thus results in lesser total energy production.

Specifically, according to Figure 5.28, wells on dip direction produce from 0.80e13 to approximately 1.75e13 KJ over its life time, while wells on strike direction produce from 0.90e13 to 1.80e13 KJ with the elimination of outliers. These numbers are almost two times smaller than that of the base case, which ranges from 1.5e13 to 3.75e13 KJ for the total net energy production.



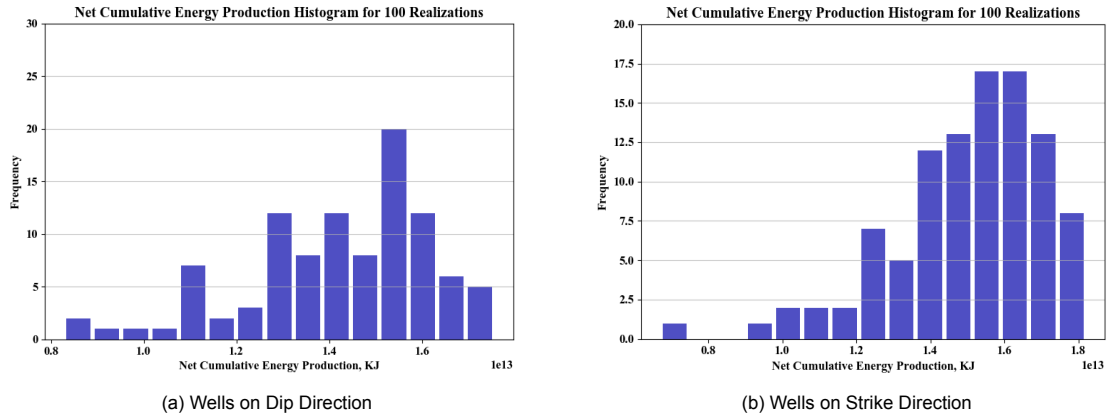(a) Wells on Dip Direction

(b) Wells on Strike Direction

Figure 5.28: Gravity Model Ensemble Simulations Net Energy Production Histogram

With less than half of the total energy production in comparison to the base case, the economic viability of the project also diminishes. The histograms below in Figure 5.29 indicates that for both cases the project is not profitable. Moreover, for the scenario with wells drilled on dip direction on the fault plane, the drilling depth for the injection well is 600 m shallower than the producer, resulting in a reduction of capital expense of 1.82E6 Euros as well as fixed operation expense. This means that the NPV value for dip case is greater than that of the strike case, providing economic incentive for such well couplet configuration. Specifically, the NPV ranges from -0.5e7 to 0.2e7 Euros for the dip case, while this range is -1.2e7 to -0.4e7 Euros for the strike case.



(a) Wells on Dip Direction
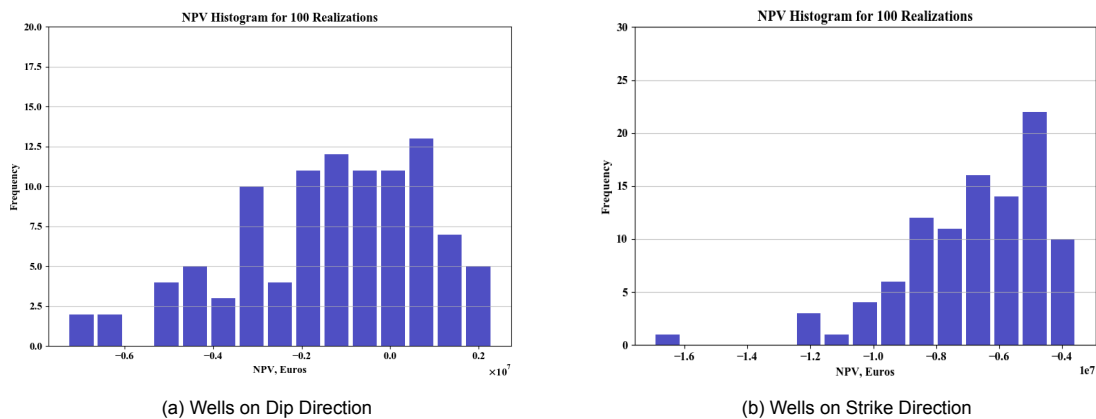
(b) Wells on Strike Direction

Figure 5.29: Gravity Model Ensemble Simulations NPV Results

6

# Conclusion and Recommendations

## 6.1. Conclusion

For faulted deep geothermal systems, the aperture distribution within the fracture plane plays an important role in determining the total energy production over lifetime and raises potential risk for the economic outcome of investment. With the implementation of aperture change from the state of rock stress, which is equal to overburden stress minus fluid pressure, it is observed that total net energy production changes to a maximum extent of 1% due to the reduced reservoir pressure over time and pressure gradient between injector and producer, both of which have little to no effect on aperture or permeability enhancement due to the non-linear pressure-permeability dependence function utilized in the model. However, it is important to mention that the aperture changes are made based on the simplified representation and full geomechanical analysis may change this conclusion.

For the base case, the well is positioned in a strike configuration at the bottom of the model - granitic layer. With the stress-induced aperture change taken into account, all four analyzed parameters demonstrate a wide variability of the results over 100 simulations. Without obvious outliers, the pressure difference between injector and producer ranges from 20 to 80 bar, and the end production temperature sees a maximum difference of 35 K among the ensemble of simulations. More importantly, the maximum value for the total energy production is more than two times higher than the minimum, which results in a widespread NPV distribution whose variability range is close to 4.

From the sensitivity analysis, a few major components are investigated to observe their impact on the model parameters outcome. These components are well spacing, well position configuration (relative to fault orientation), and gravity effect. It is found out that with half of the well spacing in comparison to the base case, despite the overall reduction of produced energy due to the lesser total enthalpy in the flow path, the range or spread of the net energy production results is slightly greater than that of the base case. The same trend can also be observed in other parameters such as production temperature. This is because the shorter well spacing yields the shorted flow path and the results become more sensitive to the aperture or permeability distribution. Therefore, under identical fracture aperture distribution, well spacing has considerable impact on the outcome prediction and increases uncertainties.

Gravity effect is crucial for cases with well configuration along the dip direction as now the injector and producer are placed at different depth. Another aspect of gravity model is the non-uniform pressure and temperature distribution based on the corresponding gradient and cell depth within the model - instead of populating a singe temperature and pressure value for all cells, the reservoir should demonstrate a gradient of temperature and pressure with changing depth. With these factors considered, two well configurations are tested, which are along the dip and along the strike. The net energy production results indicate an almost identical maximum to minimum value ratio as the base. However, due to the temperature gradient and the diversion of flow due to the gravity in the strike orientation case, the produced energy is nearly twice smaller than that of the base case, which implies the importance of

taking into account gravity effect.

In summary, the outcome of deep geothermal production greatly depends on the degree of fault heterogeneity and its aperture distributions. The stress dependent aperture and permeability cause little no significant effect with the conditions tested in the model. With ensemble simulation of 100 realizations, although the statistics value of fracture aperture distribution remain identical, the varying permeability in the flow path between the wells can alter the production results up to 200 % difference in relative to the minimum value. For the sensitivity analysis without gravity effect, the range of energy production results is similar with the values offset based on the specific scenario. It is also important to acknowledge the essential role of gravity effect as it not only reduces the spread of energy production outcome but also decreases the overall energy production due to the temperature gradient distribution and flow deviation from the original flow path without gravity. Therefore, the knowledge of fracture permeability distribution in the geothermal reservoir such as its order of magnitude variation and potential permeable barrier should be collected for a more accurate prediction of geothermal project production.

## 6.2. Recommendations

A few more points should be considered for further improvement of what comes from this report as well as more accurate reservoir representation and thorough sensitivity analysis.

- Fault aperture changes based on thermal stresses.

- Fault groups with faults of difference length and orientation to see the role of interaction among the faults.

- Fault offset or displacement that may cause different characteristics at each layer within the fracture.

- More than one producer and one injector to test the sensitivity of fracture aperture distribution with more well doublets.

- Detailed mechanic properties for matrix and fracture rock to depict the stress state more accurately.

- Different type of pressure-permeability correlation function.

- Two-phase model in the reservoir that includes steam phase, as in this report only water phase is present under the determined conditions (see Appendix).

# 7

# Bibliography

1. Albert Genter, Keith Evans, Nicolas Cuenot, Daniel Fritsch, Bernard Sanjuan, Contribution of the exploration of deep crystalline fractured reservoir of Soultz to the knowledge of enhanced geothermal systems (EGS), Comptes Rendus Geoscience, Volume 342, Issues 7–8, 2010, Pages 502-516, ISSN 1631-0713, https://doi.org/10.1016/j.crte.2010.01.006. [Accessed 1 Feb 2020]

2. Baujard C., Genter A., Cuenot N., Mouchot J., Maurer V., Hehn R., Ravier G., Seibel O., Vidal J.: Experience from a successful soft stimulation and operational feedback after 2 years of geothermal power and heat production in Rittershoffen and Soultz-sous-Forêts plants (Alsace, France), Geothermal Resource Council, GRC2018, October 14-17, Reno, Nevada, USA, 2241-2252. [Accessed 4 April 2020]

3. C. Baujard, A. Genter, E. Dalmais, V. Maurer, R. Hehn, R. Rosillette, J. Vidal, J. Schmittbuhl, Hydrothermal characterization of wells GRT-1 and GRT-2 in Rittershoffen, France: Implications on the understanding of natural flow systems in the rhine graben, Geothermics, Volume 65, 2017, Pages 255-268, ISSN 0375-6505, https://doi.org/10.1016/j.geothermics.2016.11.001. [Accessed 5 April 2020].

4. C. Baujard, A. Genter, E. Dalmais, V. Maurer, R. Hehn, R. Rosillette, J. Vidal, J. Schmittbuhl, Hydrothermal characterization of wells GRT-1 and GRT-2 in Rittershoffen, France: Implications on the understanding of natural flow systems in the rhine graben, Geothermics, Volume 65, 2017, Pages 255-268, ISSN 0375-6505, https://doi.org/10.1016/j.geothermics.2016.11.001. [Accessed 20 January 2020].

5. Bine.info. n.d. http://www.bine.info. [Accessed 24 March 2020].

6. da Silva, J. A., Kang, P. K., Yang, Z., Cueto☐Felgueroso, L., … Juanes, R. (2019). Impact of confining stress on capillary pressure behavior during drainage through rough fractures. Geophysical Research Letters, 46, 7424– 7436. https://doi.org/10.1029/2019GL082744 [Accessed 28 November 2019].

7. Daniilidis, A., Alpsoy, B., and Herber, R. (2017). Impact of technical and economic uncertainties on the economic performance of a deep geothermal heat system. Renewable Energy, 114(Parat B):805–816. [Accessed 16 October 2020].

8. Daniilidis, A. Saeid, S. Doonechaly, G. Fault plane as the main fluid pathway: an exploration of field development options under uncertainty based on the Rittershoffen geothermal field [Accessed 20 April 2020].

9. Denis V. Voskov, Operator-based linearization approach for modeling of multiphase multi-component flow in porous media, Journal of Computational Physics, Volume 337, 2017, Pages 275-288, ISSN 0021-9991, https://doi.org/10.1016/j.jcp.2017.02.041. [Accessed 15 May 2020].

10. Ec.europa.eu. 2009. GEOTHERMAL REGULATION FRAMEWORK.[Accessed 4 September 2020]

11. 2008. ECLIPSE Technical Description 2008. 2nd ed. p.1123.[Accessed 15 October 2020].

12. Environment.uwe.ac.uk. n.d. Vertical Stress In The Ground. [Accessed 20 May 2020].

13. Flodin, Eric & Durlofsky, Louis & Wen, Xian-Huan. (2002). Computing permeability of fault zones in eolian sandstone from outcrop measurements. AAPG Bulletin. 86. [Accessed 28 June 2020]

14. Geoenvi.brgm.fr. 2020. Soultz-Sous-Forets | Satellite D8 [En]. https://geoenvi.brgm.fr/en/node/2001. [Accessed 28 January 2020].

15. GitHub. 2018. Cphyc/Fyeldgenerator. https://github.com/cphyc/FyeldGenerator [Accessed 28 June 2020].

16. IAPWS R7-97(2012): IAPWS-IF97 Industrial Formulation for Thermodynamic Properties of Water and Steam. (n.d.). Retrieved March 12, 2020, from http://www.iapws.org/relguide/IF97-Rev.html. [Accessed 13 Marcha 2020]

17. Investopedia. 2019. "What Is The Formula For Weighted Average Cost Of Capital (WACC)" [Accessed 14 October 2020]

18. Investopedia. 2020. Net Present Value (NPV). https://www.investopedia.com/terms/n/npv.asp. [Accessed 14 October 2020].

19. Jeanne Vidal, Albert Genter, Overview of naturally permeable fractured reservoirs in the central and southern Upper Rhine Graben: Insights from geothermal wells, Geothermics, Volume 74, 2018, Pages 57-73, ISSN 0375-6505, https://doi.org/10.1016/j.geothermics.2018.02.003.[Accessed 28 January 2020]

20. Jon Jincai Zhang, Chapter 2 - Rock physical and mechanical properties, Editor(s): Jon Jincai Zhang, Applied Petroleum Geomechanics, Gulf Professional Publishing, 2019, Pages 29-83, ISBN 9780128148143, https://doi.org/10.1016/B978-0-12-814814-3.00002-2.[Accessed 18 May 2020].

21. Kasalsenergiebron.nl. 2013. Winning Aardwarmte Voor Glastuinbouw. [Accessed 16 October 2020].

22. Khait, M. (2019). Delft Advanced Research Terra Simulator: General Purpose Reservoir Simulator withOperator-Based Linearization. https://doi.org/10.4233/uuid:5f0f9b80-a7d6-488d-9bd2-d68b9d7b4b87. [Accessed 15 December 2019].

23. Luo, Jin & Zhu, Yongqiang & Guo, Qinghai & Tan, Long & Zhuang, Yaqin & Liu, Mingliang & Zhang, Canhai & Xiang, Wei & Rohn, Joachim. (2017). Experimental investigation of the hydraulic and heat-transfer properties of artificially fractured granite. Scientific Reports. 7. 10.1038/srep39882. [Accessed 12 June 2020]

24. Maurer, Vincent & Aichholzer, Coralie & Richard, Alexandre & Pauline, Harlé & Hehn, Régis & Genter, Albert & Duringer, Philippe. (2018). Geothermal reservoir temperature estimation derived from gradient wells in a continental rift context (Upper Rhine Graben). [Accessed 23 October 2020].

25. Moucho, J., Genter, A., Cuenot, N., Scheiber, J. and Seibel, O., 2018. First Year Of Operation From EGS Geothermal Plants In Alsace, France: Scaling Issues. [Accessed 3 February 2020].

26. Mouchot, J., Ravier, G., Seibel, O. and Pratiwi, A., 2019. Deep Geothermal Plants Operation In Upper Rhine Graben: Lessons Learned. Europeangeothermalcongress.eu. [Accessed 18 October 2020].

27. Neuweiler, Insa, Sorensen, Ivan, Kinzelbach, Wolfgang. (2004). Experimental and theoretical investigations of drainage in horizontal rough-walled fractures with different correlation structures. Advances in Water Resources. 27. 1217-1231. 10.1016/j.advwatres.2004.07.005.[Accessed 23 November 2019].

28. Neutrium.net. 2020. Pump Power Calculation | Neutrium. [Accessed 14 October 2020].

29. Philippe Duringer, Coralie Aichholzer, Sergio Orciani, Albert Genter; The complete lithostrati-graphic section of the geothermal wells in Rittershoffen (Upper Rhine Graben, eastern France): a key for future geothermal wells. Bulletin de la Société Géologique de France ; 190 (1): 13. doi: https://doi.org/10.1051/bsgf/2019012. [Accessed 1 May 2020].

30. Portier, N., Hinderer, J., Riccardi, U. et al. New results on the gravity monitoring (2014–2017) of Soultz-sous-Forêts and Rittershoffen geothermal sites (France). Geotherm Energy 6, 19 (2018). https://doi.org/10.1186/s40517-018-0104-5.[Accessed 4 July 2020]

31. Ravier, G., 2020. Rittershoffen Geothermal Heat Plant. Geoenvi.eu.[Accessed 28 June 2020]

32. Rijksoverheid.nl. 2020. Aanpassing Lage Tarief Vennootschapsbelasting En Schijven. [Accessed 4 September 2020]

33. Ronald DiPippo, Chapter 22 - Enhanced Geothermal Systems—Projects and Plants, Editor(s): Ronald DiPippo, Geothermal Power Plants (Fourth Edition), Butterworth-Heinemann, 2016, Pages 609-656, ISBN 9780081008799, https://doi.org/10.1016/B978-0-08-100879-9.00022-7. [Accessed 9 December 2019].

34. Sadiq J. Zarrouk, Hyungsul Moon, Efficiency of geothermal power plants: A worldwide review, Geothermics, Volume 51, 2014, Pages 142-153, ISSN 0375-6505. [Accessed 21 October 2020].

35. Spijker, H. and Ungemach, P., 2016. Definition Of Electrosubmersible Pump (ESP) Design And Selection Workflow. Geothermie.nl. [Accessed 19 October 2020].

36. Statista. 2020. Industrial Prices For Electricity In The Netherlands 1995-2019 | Statista. [Accessed 15 October 2020].

37. Stichting Platform Geothermie. (2018). Master Plan Geothermal Energy In The Netherlands. https://geothermie.nl/images/bestanden/ Masterplan_Aardwarmte_in_Nederland_ENG.pdf. [Accessed 16 November 2019].

38. ThermoGIS. n.d. https://www.thermogis.nl/en/geothermal-family. [Accessed 8 December 2019].

39. ThermoGIS. 2020. Economic Model. https://www.thermogis.nl/en/economic-model. [Accessed 16 October 2020].

40. Thorsteinsson H, Augustine C, Anderson BJ, Moore MC, Tester JM. The impacts of drilling and reservoir technology advances on EGS exploitation. Proceedings of the 33rd workshop on geother-mal reservoir engineering. Stanford University, Stanford, CA; 2008, SGP-TR-18.[Accessed 9 December 2019].

41. van der Welle, A. and Lensing, S. (2018). Conceptadvies SDE+ 2019. Overzicht basisbedra-gen en algemene parameters en uitgangspunten. Publicatienummer 3300, Planbureau voor de leefomgeving.[Accessed 15 October 2020]

42. Wu, H., Fu, P., Morris, J. P., Settgast, R. R., Ryerson, F. J., Mattson, E. D., … Zhang, Y. (2019, August 28). Stochastic Modeling of a Conservative Tracer Test for the Characterization of Frac-ture Flow Patterns in EGS Collab Experiment 1. American Rock Mechanics Association [Accessed 22 November 2019].

43. Yang, Zhibing & Niemi, Auli & Fagerlund, Fritjof & Illangasekare, T.. (2012). A generalized ap-proach for estimation of in-plane curvature in invasion percolation models for drainage in frac-tures. Water Resour. Res.. 48. W09507. 10.1029/2012WR011829. [Accessed 22 November 2019].

44. Zaal, C., 2020. Geothermal Field Development Strategies Based On Economic And Fault Stability Analysis. MSc. Delft University of Technology.[Accessed 15 October 2020]

# A
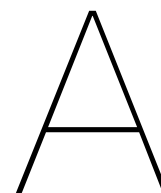
# Appendix: NPV Model Workflow

| Time Period | 0 | 1 | 2 | 3 | 4 |
|---|---|---|---|---|---|
| Pumping Energy (KJ) | 0 | 2.15E+09 | 2.04E+09 | 2.04E+09 | 2.03E+09 |
| Heat Production (KJ) | 0 | 2.72E+11 | 2.44E+11 | 2.33E+11 | 2.26E+11 |
| Converted Electricity Production (KJ) | 0 | 3.54E+10 | 3.17E+10 | 3.03E+10 | 2.94E+10 |
| Heat Revenue | 0 | 688706 | 616427 | 590056 | 571122 |
| -OPEX, Fixed | 0 | (100400) | (100400) | (100400) | (100400) |
| -OPEX, Variable | 0 | (56044) | (53328) | (53206) | (53098) |
| Net Income | 0 | 532262 | 462699 | 436450 | 417625 |
| -CAPEX (Wells) | (10250000) | 0 | 0 | 0 | 0 |
| -CAPEX (Equipment) | (2300000) | 0 | 0 | 0 | 0 |
| Cash Flow | (12550000) | 532262 | 462699 | 436450 | 417625 |
| Discounted Cash Flow | (12550000) | 524648 | 449555 | 417986 | 394235 |
| Cum. Disc. Cash Flow | (12550000) | (12025352) | (11575797) | (11157811) | (10763576) |

All Currency Value in Euros

Figure A.1: NPV Model Workflow Example

B

# Appendix: Gravity Model Validation

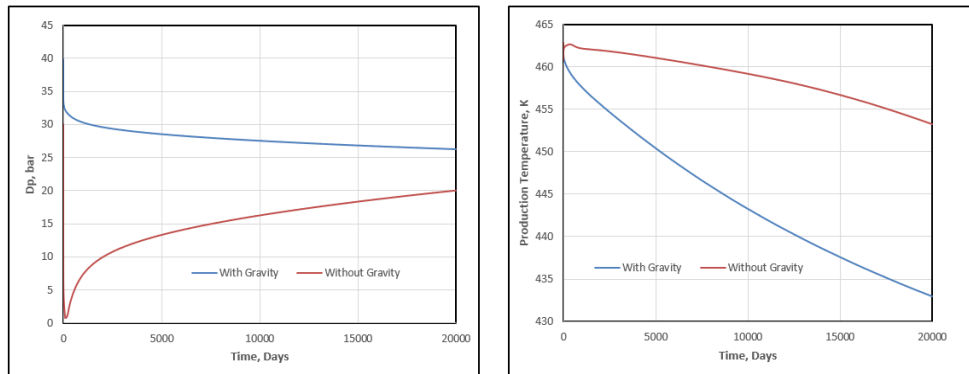## B.1. Results Comparisons for Model with/without Gravity Effect



Figure B.1: Pressure Different and Production Temperature with/without Gravity
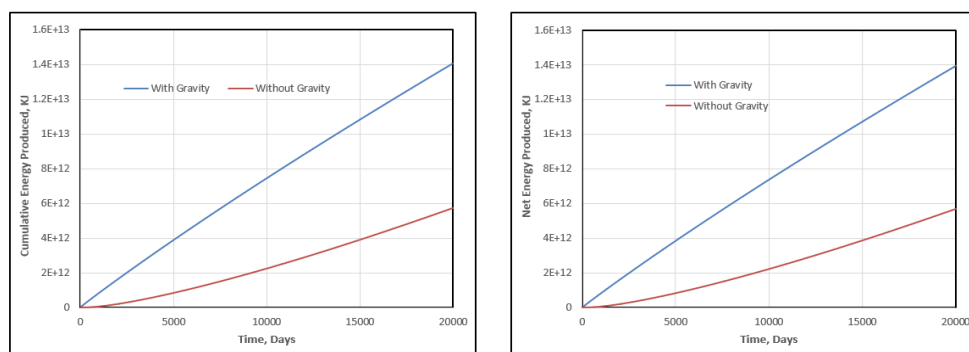
.



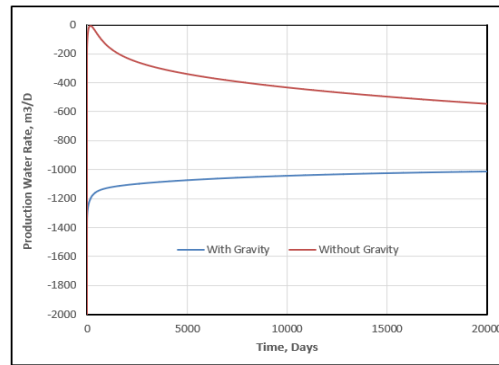Figure B.2: Energy Production with/without Gravity

Figure B.3: Production Water Rate with/without Gravity

As expected, with gravity-assisted flow the net energy production is greater at the end. Moreover, the production temperature with gravity effect is much lower than that of the case without gravity. This is because the production water rate is much greater with the gravity-assisted flow as Figure B.3 shows, and therefore the enthalpy around producer blocks depletes much faster than the case without gravity effect.

# C

# Appendix: Model Phase Behavior

The following diagram is obtained from IAPWS97 (International Association for the Properties of Water and Steam) documentation (IAPWS, 1997).
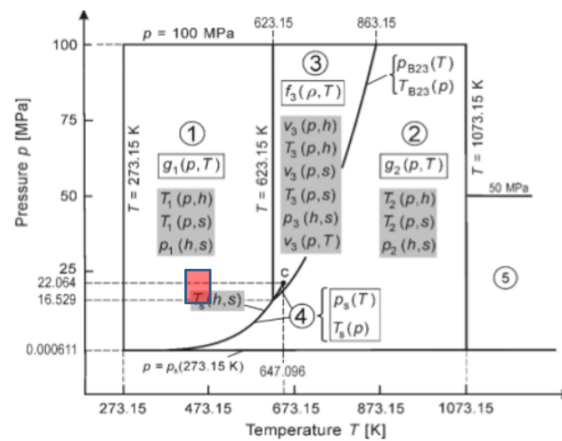


Figure C.1: PT Condition for Model Simulations

The red area is the pressure and temperature range for all simulation cases. As it can observed, the condition is always in Region 1, which by definition means water saturation is 1 and steam saturation equals to 0 (IAPWS, 1997).